Energy nonequipartition, rheology and microstructure in sheared bidisperse granular mixtures

Meheboob Alam [*]

Engineering Mechanics Unit, Jawaharlal Nehru Center for Advanced

Scientific Research, Jakkur P.O., Bangalore 560064, India

Stefan Luding

Particle Technology, DelftChemTech, TU-Delft, Julianalaan 136

2628 BL Delft, The Netherlands

May 2, 2005

ABSTRACT: Event driven simulations of smooth inelastic hard-disks are used to probe the transport properties and the microstructure of bidisperse granular mixtures. A generic feature of such mixtures is that the two species

_____
[*]To whom correspondence should be addressed: Email: meheboob@jncasr.ac.in

1

have different levels of fluctuation kinetic energy ($T_l \neq T_s$) in contrast to their elastic counterpart. The microscopic mechanism for this energy non-equipartition is shown to be directly tied to the *asymmetric* nature of collisional probabilities between the heavier and lighter species, compared to their purely elastic counterpart. The degree of collisional asymmetry increases with both increasing inelasticity and mass-disparity, thereby increasing the energy ratio T_l/T_s in the same limit. A phenomenological constitutive model, that incorporates energy *non-equipartition*, captures the *non-monotonic* behaviour of the transport coefficients, in agreement with simulation results, whereas the standard constitutive model with equipartition assumption predicts *monotonic* variations. The sheared granular mixture readily forms clusters, having striped-patterns along the extensional-axis of the flow. The microstructural flow-features are extracted by measuring the cluster-size distributions, the pair correlation function and the collision-angle distribution. While the inelastic dissipation is responsible for the onset of clustering, we have found that the mass-disparity between the two species enhances the degree of clustering significantly in the sense that the size of the largest cluster increases with increasing mass-disparity. At the microscopic-level, the particle motion becomes more and more *streamlined* (i.e. *ordered* along the streamwise direction which is also a signature of enhanced *short-range correlations*) with increasing dissipation and mass-disparity, which is responsible

2

for the enhanced first normal stress difference in the same limit.

1 Introduction

The majority of the rheological studies on granular materials are confined to *monodisperse* systems, where the particles are of the same density and size[1, 2, 3, 4, 5]. In practice, however, a granular system is rarely monodisperse, but is always characterized by some degree of *polydispersity* in density and size. An associated phenomenon in a driven granular mixture is the spontaneous segregation of an otherwise homogeneous mixture which could be a nuisance in many processing industries. For example, a granular mixture, under vertical-vibrations or in a rotating drum, segregates according to size and/or mass[6, 7, 8, 9, 10]. The bulk-rheology of a homogeneous mixture is likely to differ from that of a partially segregated-one, and hence it is of interest to study the rheology of granular mixtures.

From a more fundamental viewpoint, prior understanding of the rheology is important to make meaningful progress in developing constitutive models. The major objective of the present work is to understand the bulk-rheology and microstructural features of granular mixtures and the influence of various control parameters on them. Another objective is to propose a simplified constitutive model and validate the same against the rheological data obtained from simulations.

Drawing an analogy with the dense-gas kinetic theory of mixtures[11, 12, 13], several constitutive models for bidisperse granular mixtures have been proposed[14, 15, 16, 17, 18]

All these models are first-order in inelasticity, meaning that they are valid for nearly elastic particles. Another important assumption in these models is that the fluctuation energy is *equally* partitioned between two species. One way to validate these theories is to perform simple rheological *experiments* via particle-level simulations. Some effort in this direction has been made by the present authors[17, 19, 20] who carried out event-driven simulation of bidisperse granular mixtures, characterized by both size- and mass-disparities, under uniform shear flow. The overall effect of such bidispersities is to enhance the non-Newtonian character of the fluid in the sense that the first normal stress difference (i.e. the diagonal components of the stress tensor are not equal) increases as the degree of bidispersity increases.

It has been recently found[18, 19, 20, 21, 22, 23, 24, 25, 26, 27] that the granular energy is *not* equally partitioned between the two species, an example of which is shown in Fig. 1 for a sheared binary granular mixture (see Appendix A for simulation details). This figure shows the time evolution of the granular energy, T_α, of species α, defined as:

$$T_\alpha = < m_\alpha \mathbf{C}_\alpha^2 > = < m_\alpha (\mathbf{c}_\alpha - \mathbf{u})^2 >, \quad \text{with} \quad \alpha = l, s. \qquad (1)$$

Here $\mathbf{u}$ is the mass-averaged velocity of the mixture, $\mathbf{c}_\alpha$ is the instantaneous velocity of particles of species α and $\mathbf{C}_\alpha$ is the peculiar velocity. Note that the subscript l (or s) is used to denote a species which is *larger* (or *smaller*) in mass and size. For this plot, the particles are of the same size

5

$(R = R_{ls} = d_l/d_s = 1.0)$ with a mass-ratio of $R_m = m_l/m_s = 9.0$, the mean volume fraction is $\nu = \nu_l + \nu_s = 0.05$ with $\nu_l = \nu_s$, and the coefficient of restitution is $e = 0.9$. The granular energies of two species are clearly unequal with the energy ratio being $R_T = T_l/T_s = 1.67 \pm 0.12$. *Thus, the principle of equipartition of energy does not hold for a granular mixture and this adds another peculiar property to granular fluids in contrast to their molecular counterpart.* Even though the inelasticity is responsible for the *onset* of energy non-equipartition[18, 22], it is the *mass-disparity* which strongly amplifies this energy non-equipartition[19, 20].

The microscopic mechanism for energy non-equipartition is unveiled in §2 by probing the collision probabilities between different species. We use the well-known smooth inelastic hard-disk model for event-driven simulations[28] of the uniform shear flow, the details of which are described in Appendix A. The simulation results on the rheological properties, along with their comparisons with the predictions of a phenomenological constitutive model, are presented in §3. The phenomenological constitutive model[19] which takes into account the non-equipartition of granular energy is detailed in Appendix B. The effect of mass-disparity on the non-Newtonian behaviour is presented in §3.2. The microstructural features of bidisperse mixtures and their impact on the macroscopic rheological fields are described in §4. In §5 we summarize our findings, and close with suggestions for possible future work.

2 Mechanism for energy non-equipartition

As mentioned in the Introduction, the inelastic dissipation is responsible for energy non-equipartition [18, 19, 20, 21, 22, 23, 24, 25] and the mass-disparity between the two species amplifies the magnitude of this non-equipartition significantly [19, 20]. However, it is not clear how the energy dissipation at the particle-level leads to the breakdown of the equipartition principle.

To probe the underlying *microscopic mechanism* for energy non-equipartition, we meassure the following quantity from our simulations:

$$\Omega_{\alpha\beta} = \frac{Number\ of\ collisions\ between\ species\ \alpha\ and\ \beta}{Total\ number\ of\ collisions}$$

such that $\sum_\alpha \sum_\beta \Omega_{\alpha\beta} = 1$. Note that $\Omega_{\alpha\beta}$ is nothing but the probability of collisions between species α and β. Figure 2 shows the variation of $\Omega_{\alpha\beta}$ with the mass-ratio for a low-density mixture with parameter values set to $\nu = 0.05$, $\nu_l = \nu_s$, $e = 0.9$ and $R = 1$. Note that for this case both the species have equal number of particles ($N_l = N_s$), and it is straightforward to verify that $\Omega_{ll} = \Omega_{ss} = \Omega_{ls} = 0.25$ at $R_m = 1$. We observe that while both Ω_{ss} and Ω_{ls} remain relatively uniform with increasing mass-ratio, Ω_{ll} decreases sharply in the same limit. The collision probability can be identified with species granular energies in the following way: the larger the value of $\Omega_{\alpha\alpha}$, the larger is the collisional energy dissipation rate among the particles of species α, which in turn would lower the granular energy of species α. Since

the number densities of the two species are equal in Fig. 2, the effect of the cross term $\Omega_{\alpha\beta}$ on increasing/decreasing the species granular energy would be the same for both species. For this case, we can define the *effective* collision probability of species α as

$$\Omega_\alpha = \Omega_{\alpha\alpha} + \Omega_{\alpha\beta}, \quad \text{with} \quad \alpha \neq \beta, \tag{2}$$

whose variation with mass-ratio, R_m, is plotted in the inset of Fig. 2. (In this definition, we do not take into account the difference of energy loss of each species after their collision.) It is observed that while the effective collision probability of the lighter particles increases with R_m, that of the heavier particles decreases in the same limit. This implies that the lighter particles will lose kinetic energy (through collisional dissipation) much more rapidly than the heavier particles as the mass-ratio is increased, and this clearly yields $T_l > T_s$, leading to the non-equipartition of granular energy.

Now to understand the departure from a purely *elastic* hard-disk mixture (for which the equipartition principle holds, i.e. $T_l = T_s = T$), we derive an analytical expression for $\Omega_{\alpha\beta}$. In the dilute limit, the number of collisions per unit area and time between pairs of elastic disks of species α and β is given by[11]

$$N^c_{\alpha\beta} = n_\alpha n_\beta d_{\alpha\beta} \sqrt{\frac{2\pi T}{\mu_{\alpha\beta}}}, \tag{3}$$

where n_α is the number density of species α, $\mu_{\alpha\beta} = m_\alpha m_\beta/(m_\alpha + m_\beta)$ the reduced mass and $d_{\alpha\beta} = (d_\alpha + d_\beta)/2$. Thus, the probability of collisions

8

between species α and β is

$$\Omega_{\alpha\beta}^E = \frac{N_{\alpha\beta}^c}{\sum N_{\alpha\beta}^c} = \frac{d_{\alpha\beta}\mu_{\alpha\beta}^{-1/2}N_\alpha N_\beta}{\sum_{\alpha=l,s}\sum_{\beta=l,s} d_{\alpha\beta}\mu_{\alpha\beta}^{-1/2}N_\alpha N_\beta} \tag{4}$$

where the superscript E is used to denote the purely elastic mixture ($e_{\alpha\beta} = 1$). Note that for mechanically equivalent particles ($R = 1$ and $R_m = m_l/m_s = 1$), this expression reduces to

$$\Omega_{\alpha\beta}^E(R = 1, R_m = 1) = \frac{N_\alpha N_\beta}{N^2}. \tag{5}$$

We can normalize our simulation data for the effective collision probability, Ω_α, (see inset of Fig. 2) by its theoretical value (4) for the elastic case:

$$\Omega_\alpha^* = \frac{\Omega_\alpha}{\Omega_\alpha^E}. \tag{6}$$

This *normalized* quantity is unity for a binary mixture of purely elastic particles. Now we define the *effective collision ratio* (between species l and s) as the ratio between the two normalized effective collision probabilities of species l and s:

$$R_\Omega = \frac{\Omega_l^*}{\Omega_s^*} = \left(\frac{\Omega_l}{\Omega_l^E}\right)\Big/\left(\frac{\Omega_s}{\Omega_s^E}\right). \tag{7}$$

Note that R_Ω is also unity for a binary mixture of elastic particles and its departure from unity will signal the breakdown of the equipartition principle. The departure of R_Ω from unity can also be thought of as the collisions being *asymmetric* in the sense that one species collides more frequently than the other, compared to their elastic counterparts.

9

The variation of the effective collision ratio, R_Ω, with the mass-ratio, R_m, is shown in Fig. 3 for two different values of the restitution coefficient. The other parameter values are as in Fig. 2. It is observed that R_Ω increases with increasing R_m and decreasing e. In other words, the asymmetry between Ω_l^* and Ω_s^* increases as the mass-disparity and inelasticity increase. The inset of Fig. 3 displays the variation of the granular energy ratio, $R_T = T_l/T_s$, with R_m. Similar to R_Ω, the energy ratio R_T increases with both increasing mass-ratio and inelasticity. This observation suggests that the departure of the effective collision ratio R_Ω from unity is directly tied with the breakdown of the equipartition principle ($R_T \neq 1$). Thus, we can conclude that the microscopic mechanism for energy non-equipartition is directly tied to the *asymmetric* nature of collision probabilities between the two species, compared to their elastic counterparts.

3   Rheological properties of uniform shear flow

For the steady ($\partial/\partial t(.) = 0$), fully developed ($\partial/\partial x(.) = 0$) plane shear flow of a binary mixture of granular material, it is easy to verify that a linear streamwise velocity profile along with constant density and constant granular energy satisfies the balance equations[20]. Thus, the mean fields (in dimensionless form, see Appendix A for the reference non-dimensional

quantities) are given by

$$
\left.
\begin{aligned}
\nu &= \textstyle\sum_{\alpha=l,s} \nu_\alpha = \text{const.} \\
T &= \textstyle\sum_{\alpha=l,s} \xi_\alpha T_\alpha = \text{const.} \\
\mathbf{u} &\equiv (u,v)^T = (y,0)^T
\end{aligned}
\right\}
\qquad (8)
$$

where $\xi_\alpha = n_\alpha/(n_l + n_s)$ is the number fraction of species α and n_α is its number density. Note that we nondimensionalize the granular energy and the stress by the species-averaged kinetic energy and momentum flux density, respectively, as in eqn. (A.4). An expression for the dimensionless species granular energy T_α is obtained from the energy balance equation, by equating the production term due to shear-work $(-\mathbf{P}{:}\nabla\mathbf{u})$ with collisional dissipation $(\tilde{\mathcal{D}})$:

$$
T_\alpha = \frac{\sum_{\beta=l,s} \sqrt{\frac{T_\beta}{T_\alpha}} f_{2\beta} \sqrt{\frac{\rho_\beta}{\rho_l}}}{\sum_{\beta=l,s} \left(\frac{T_\beta}{T_\alpha}\right)^{3/2} f_{5\beta} \left(\frac{d_l}{d_\beta}\right)^4 \left(\frac{\rho_l}{\rho_\beta}\right)^{1/2} \sum_{\gamma=l,s} \frac{m_\gamma}{m_l} \chi_\gamma \left(\frac{d_\gamma}{d_l}\right)^2}, \qquad \forall \quad \alpha = l,s
\qquad (9)
$$

where $\chi_\alpha = \nu_\alpha/(\nu_l + \nu_s)$ is the relative volume fraction of species α. The dimensionless expressions for pressure and shear viscosity are

$$
p = \sum_{\alpha=l,s} p_\alpha = \frac{\sum_{\alpha=l,s} f_{1\alpha} T_\alpha \sum_{\beta=l,s} \frac{m_\beta}{m_l} \chi_\beta \left(\frac{d_\beta}{d_l}\right)^2}{\sum_{\beta=l,s} \frac{\rho_\beta}{\rho_l} \chi_\beta \left(\frac{d_\beta}{d_l}\right)^2}
\qquad (10)
$$

$$
\mu = \sum_{\alpha=l,s} \mu_\alpha = \frac{\sqrt{\pi} \sum_{\alpha=l,s} \sqrt{\frac{\rho_\alpha}{\rho_l}} f_{2\alpha} T_\alpha^{1/2} \sqrt{\sum_{\beta=l,s} \frac{m_\beta}{m_l} \chi_\beta \left(\frac{d_\beta}{d_l}\right)^2}}{2 \sum_{\beta=l,s} \frac{\rho_\beta}{\rho_l} \chi_\beta \left(\frac{d_\beta}{d_l}\right)^2}, \qquad (11)
$$

where $f_{1\alpha}$, $f_{2\alpha}$ and $f_{5\alpha}$ are functions of the mixture parameters ν_α, $M_{\alpha\beta}$, etc., as defined in Appendix B. Simulation results on pressure, viscosity and

11

granular energy will be compared with the above expressions.

3.1 Comparison between simulation and theory

From the event-driven simulations of smooth inelastic hard-disks under uniform shear flow, we measure pressure, shear viscosity, granular energy and the first normal stress difference. The simulation details and the definitions of different transport coefficients are provided in Appendix A. There are five dimensionless control parameters in this problem: the total solid volume fraction (ν), the relative volume fraction of heavier/larger particles ($\chi = \nu_l/\nu$), the size ratio ($R = d_l/d_s$), the mass ratio ($R_m = m_l/m_s$), and the coefficient of normal restitution (e). Note that $\chi = 1$ corresponds to the monodisperse limit with all the heavier particles and $\chi = 0$ to the same limit but having only lighter particles. Here we mainly focus on the bidisperse mixture of equal size particles ($R = d_l/d_s = 1$), characterized by density or mass-disparity, with the goal to understand the effect of mass-disparity on its rheology.

3.1.1 Pressure, viscosity and granular energy

Figure 4 shows the variations of pressure, viscosity and granular energy with the mass-ratio for a dilute mixture ($\nu = 0.01$) of *equal-size* particles; other parameters are set to $\chi = 0.5$ and $e = 0.9$. The model predictions are denoted by lines and the simulation data by symbols. In the limit of $e \to 1$ the

12

predictions are almost perfect (data not shown here) so that we rather provide data for $e = 0.9$ to visualize the discrepancy. We observe that both pressure and viscosity vary *non-monotonically* with the mass-ratio. Looking at the variations of the *partial* components of pressure (p_l and p_s) and viscosity (μ_l and μ_s), we find that in the limit of large mass-ratio the transport coefficients are primarily determined from the respective contributions due to the heavier species. On the whole, our phenomenological model provides reasonable predictions for both the total and partial components of these transport coefficients. Note that the variation of the granular energy with R_m is also non-monotonic as predicted by our model. In contrast, however, the model predictions with the equipartition assumption suggest a monotonic decay of T with R_m [17, 20] as shown by the dashed line in Fig. 4(c).

The variations of pressure, viscosity and their partial components for a wide range of solid fractions are displayed in Fig. 5. Panels in the top row corresponds to a mass-ratio of $R_m = 9$ and those in the bottom row corresponds to a mass-ratio of $R_m = 25$; other parameters are $R = 1$, $\chi = 0.5$ and $e = 0.9$. For both mass-ratios, the simulation results are well captured by our model over the range of solid fractions studied. It is observed from Fig. 5(a-b) that the model predictions for both pressure and viscosity are a little higher than our simulation data for $\nu \leq 0.5$, as expected. However, for high densities $\nu \geq 0.7$ the model underestimates the simulation data. This may

be attributed to our choice of the radial distribution function (B11) which diverges at $\nu = 1.0$. Another choice of the radial distribution function[22] that diverges at $\nu = \nu_{max}$ (where $\nu_{max} = \pi/2\sqrt{3}$ corresponds to the maximum regular packing limit) yields better agreement in the dense limit. Note, however, that the modified function shows deviations from the original function only at very large volume fractions $\nu > 0.6$.

To understand the non-monotonic behaviour of the pressure and viscosity with the mass-ratio, we need to recall their variations with density for a sheared monodisperse granular system. As described in the previous paragraph, the variations of both p and μ with density follow U-shaped curves, with minima occuring at a density of $\nu \approx 0.3$. Since at large enough mass-ratios ($R_m >> 1$), the lighter particles contribute little to transport properties due to their lower mass and lower fluctuation velocities, the mixture would behave as if it were composed of only heavier particles with an effective *lower* density, depending on the relative volume fraction χ. Hence both pressure and viscosity would eventually increase with increasing mass-ratio. Thus, the reason for the *non-monotonic* variations of p and μ is tied to the non-equipartition of granular energy, i.e. the two species have different levels of fluctuation velocity.

Next we show a set of results for a mixture with *different size* particles, $R = d_l/d_s = 2$, in Fig. 6. The total solid fraction is set to $\nu = 0.3$, with

other parameters as in Fig. 4. The overall variations of p, μ and T with the mass-ratio R_m and their comparison with the model-predictions mirror those in the dilute case of equal-size particles. For a comparison of these data with a constitutive model with equipartition assumption, we refer to Fig. 15 of Alam & Luding[20]. We remark that the quantitative agreement between theory and simulation at a given mass-ratio improves as $e \to 1$ and becomes worse with decreasing e.

3.2   Non-Newtonian Behaviour: First normal stress difference

Here we probe the *first normal stress difference*,

$$\mathcal{N}_1 = \frac{(\sigma_{xx} - \sigma_{yy})}{p}, \tag{12}$$

of sheared granular mixtures. Note that a non-zero $\mathcal{N}_1$ is a measure of the non-Newtonian flow behaviour; $\mathcal{N}_1$ also measures the deviation of the orientation of the major principal stress away from $135°$, the compressive shear direction.

The variation of $\mathcal{N}_1$ with the mass-ratio is shown in Fig. 7(a). The total solid fraction is set to $\nu = 0.3$, and the restitution coefficient is $e = 0.9$; other parameters are $\chi = 0.5$ and $R = 1$. It is observed that $\mathcal{N}_1$ increases with increasing both the mass-ratio and the dissipation-level. In particular, the

latter observation is similar to its monodisperse counterpart[20].

The variation of $\mathcal{N}_1$ with solid fraction is shown in Fig. 7(b), with other parameters as in Fig. 7(a). Focussing on the dilute limit, we observe that $\mathcal{N}_1$ varies non-monotonically with the mass ratio as seen from the inset in Fig. 7(b). This is simply due to the fact that we have scaled $\mathcal{N}_1$ with pressure which varies non-monotonically with R_m (e.g., see Fig. 4). For mass-ratios $R_m < 25$, we observe in Fig. 7(b) that $\mathcal{N}_1$ is large for dilute flows and decreases sharply in the dense limit. For large enough mass-ratios ($R_m > 50$), we observe a non-monotonic variation of $\mathcal{N}_1$ with solid fraction. For all mass-ratios, $\mathcal{N}_1$ becomes *negative* at some critical value of the solid fraction in the dense limit ($\nu > 0.7$) as in the monodisperse case[30].

Decomposing $\mathcal{N}_1$ into its kinetic and collisional contributions

$$\mathcal{N}_1 = \mathcal{N}_1^k + \mathcal{N}_1^c, \qquad \text{where} \quad \mathcal{N}_1^k = \frac{\sigma_{xx}^k - \sigma_{yy}^k}{p} \quad \text{and} \quad \mathcal{N}_1^c = \frac{\sigma_{xx}^c - \sigma_{yy}^c}{p}, \quad (13)$$

we have found (data not shown here for the sake of brevity; see, for example, Fig. 14 of Alam and Luding[20]) that the relative kinetic contribution, $\mathcal{N}_1^k/\mathcal{N}_1$, increases with increasing R_m. For example at $\nu = 0.5$ and $e = 0.9$, the values of $\mathcal{N}_1^k/\mathcal{N}_1$ are 0.442, 0.473, 0.491 and 0.517 at mass-ratios of 1, 9, 25 and 100, respectively. This suggests that the kinetic mechanism of momemtum transport is more important for the enhanced normal stress difference with the mass-ratio for the range of volume fractions studied ($\nu < 0.7$). This observation is similar to our earlier findings for a bidisperse mixture of

16

particles having both size- and mass-disparities[20].

For the monodisperse system (see Fig. 2 in ref. [30]), it has been found that the kinetic contribution $\mathcal{N}_1^k$ is maximum at $\nu = 0$ and decreases monotonically to zero with increasing ν. On the other hand, the collisional contribution $\mathcal{N}_1^c$ is zero at $\nu = 0$ and increases with ν, remaining relatively constant over a substantial range of ν $(0.2 < \nu < 0.65)$; it decreases sharply with further increasing ν and becomes negative at some value of ν. Our preliminary work suggests that the critical solid fraction at which $\mathcal{N}_1$ changes its sign increases with increasing mass-disparity. Essentially, this *sign-reversal* of $\mathcal{N}_1$ is tied to the appearance of long-lived *force-chains* along the compressional axis of the flow[30]. Thus, in a bidisperse sheared granular mixture, the onset of force-chain formation would be delayed to a relatively higher density compared to its monodisperse counterpart. A detailed study of the dense-phase rheology of a bidisperse mixture is relegated to a separate study. For the monodisperse case[30], it has also been shown that the behaviour of the first normal stress difference is tied to the microstructure which we will discuss in §4.3.

4 Microstructure

Here we probe the microstructural features of bidisperse mixtures. In particular, we present results on *cluster-formation* and the influence of various system parameters on it in §4.1. Certain features on cluster-formation can be explained by looking at the pair correlation function as detailed in §4.2. The collision-angle distribution and its relation to the first normal stress difference are probed in §4.3. All the results presented in this section involve particles with both size- and mass-disparities.

Figures 8(*a-b*) show snapshots of particle distributions at the steady state for a mixture of equal-density particles for two different values of the restitution coefficient. Parameter values are set to $\nu = 0.3$, $\chi = 0.5$ and $R = 4$ (i.e. the mass-ratio is $R_m = 16$). Analogous snapshots for a mixture of equal-mass particles ($R_m = 1$) are shown in the bottom-row (*c-d*) of Fig. 8. For both mass-ratios, we observe that the particles tend to form agglomerates by grouping themselves with increasing dissipation level. Such *particle-clusters* appear to have striped-patterns, mainly oriented along the extensional axis of the flow as in the monodisperse case [31, 32, 33]. This preferred orientation of clusters is simply due to the pure-straining motion of the imposed shear field (see below for details). Clearly, these are *dissipation-induced* clusters since the particle distribution remains homogeneous in the elastic limit. Note that within a cluster the particles of both species are reasonably well-mixed (see,

for example, subplot 8b), and this will be quantified in the next subsection. Another important point is that the maximum cluster size never reaches the system-size, unlike in the *free cooling* case of granular fluids [34, 35]

Comparing Fig. 8(b) with Fig. 8(d), we find that the *degree* of clustering is relatively *weaker* for an equal-mass mixture than the equal-density case. This noteworthy effect of the mass-ratio on clustering becomes clear in Fig. 9 where we have shown the grey-map of the coarse-grained density fluctuation, $\nu'(x,y) = \nu(x,y) - \nu_{av}$, in the (x,y)-plane for both mass-ratios at $e = 0.5$. (We have subdivided the computational box into 30×30 smaller bins, and then calculated $\nu(x,y)$ in each bin by the standard procedure.) On the grey-scale, the particle-rich regions are denoted by a darker-shade and the particle-depleted regions by a lighter-shade. We note a large cluster, positioned around $(x,y) = (-0.2, 0)$, for the larger mass-ratio case in Fig. 9(a). Clearly, the particle-rich regions (i.e. clusters) are more prominent at $R_m = 16$ (Fig. 9a) than at $R_m = 1$ (Fig. 9b). Changing the size-ratio or the mean volume fraction does not appear to influence this qualitative observation. Thus, for a given size ratio and other parameters being fixed, decreasing the *mass-disparity* reduces the clustering tendency of the mixture.

19

4.1 Cluster size distribution

To obtain quantitative information on the sizes of clusters and their distributions, we used a 'burning-type' algorithm as in the work of Luding & Herrmann[34]. In this method, two particles i and j are assumed to be in contact (i.e. they belong to a specific cluster) if the following criterion is satisfied:

$$|\vec{r}_i - \vec{r}_j| \leq S_c(d_i + d_j)/2 \tag{14}$$

with the distance factor $S_c > 1$. Initially, each particle i is assigned to the cluster i of size $M_i = 1$, with the maximum number of clusters, i_{max}, being the total number of particles. After sorting all the particles in a linked-cell structure in order to enhance neighbourhood search, the cluster-identification algorithm is started by checking all particle pairs (i, j) according to the above distance-criterion. If any two particles belong to two different clusters i_1 and i_2 but satisfy the distance-criterion, then these two clusters are merged and, at the same time, the total number of clusters i_{max} is reduced by one. After examining all particles pairs (i, j), we obtain quantitative information about the size M_i of every cluster i, the number of clusters $N_c = i_{max}$ and the size of the largest cluster M_{max}. One can extract further information about the mean cluster-size, defined via

$$< M >= \frac{1}{N_c} \sum_{i=1}^{N_c} M_i \tag{15}$$

and its higher-order moments, defined in a suitable way.

Before presenting results, a brief remark about the choice of the distance factor $S_c > 1$ is necessary. A low value of S_c (say, 1.01) can detect only a dense cluster whose local packing fraction is almost equal to that of the regular close packing limit, while a high value (say, 1.5) will detect even a well-dispersed packet of particles as a cluster. For all the results reported herafter, the distance factor S_c is taken to be 1.1, which corresponds to a cluster whose local density is about $\nu \sim 0.65$. While this choice of S_c is arbitrary, the qualitative nature of results is not influenced if we choose a different value of S_c. Note that in the present scheme the size of a cluster is the number of particles in it, which can also be tied to a length scale for the largest cluster using an approximate relation: $L_{max} \approx d \left(\pi M_{max} / \nu_c \right)^{1/2}$.

The time evolutions of the maximum cluster size, M_{max}, and the mean cluster size, $< M >$, are shown in Fig. 10(a) for a mixture of equal-density particles, and those for a mixture of equal-mass particles are shown in Fig. 10(c), with other parameter values as in Fig. 8. We observe that there is a well-defined average value for both M_{max} and $< M >$. The variations of the time-averaged values of M_{max} and $< M >$ with the restitution coefficient are shown in Fig. 10(b) and Fig. 10(d) for equal-density and equal-mass particles, respectively. For both cases, the cluster size (M_{max} and $< M >$) increases with increasing dissipation level. Comparing Figs. 10(b) and 10(d),

we find that the cluster-size also increases with increasing mass-disparity which confirms our earlier visual observations in Fig. 8. This is an interesting finding since the mass-disparity between the two-species can be used to *control* the clustering process in a granular mixture.

We had noted in Figs. 10(a, c) that both M_{max} and $< M >$ show considerable fluctuations about a well-defined mean value. For example, the maximum cluster size is $M_{max} = 129.4 \pm 57.6$ for the equal-density mixture, and M_{max} can thus vary by a factor of about 3 for this case. Such large fluctuations in the cluster size are known to be generic for shear flows, arising due to the dynamic nature of cluster-cluster interaction process[31] as we discuss below. To better understand this process, we decompose the stream function for the uniform shear field, $\psi(x, y) = y^2$, into

$$\psi(x, y) = \psi_1 + \psi_2 = \frac{1}{2}(y^2 - x^2) + \frac{1}{2}(x^2 + y^2). \qquad (16)$$

The first stream function, $\psi_1(x, y) = y^2 - x^2 = const.$, represents a pure straining motion, while the second, $\psi_2(x, y) = x^2 + y^2 = const.$, represents a rigid rotation, as shown schematically in Fig. 11. Note that the above decomposition is equivalent to decomposing the shear-field into

$$\mathbf{u}(x, y) = (u, v)^T = (y, 0)^T = \frac{1}{2}[(y, x)^T + (y, -x)^T]. \qquad (17)$$

The former will stretch a given cluster along the extensional axis of the flow and compress it along the compressional axis, while the latter will rotate

22

the cluster in the clockwise direction. In a local frame of reference about the geometric center of a cluster, the cluster would rotate in the clockwise direction; hence two clusters will collide if they lie close to each other. By visualizing the snapshots of particle configurations at close time-intervals, we have observed that two nearby clusters indeed collide with each other and can merge together to give birth to a large cluster. This larger cluster subsequently gets stretched due to the straining motion of the shear field, before fragmenting into two or more smaller clusters. The combined effects of these processes, along with the kinematic advection of clusters due to the mean flow, give rise to a continuous cycle of collision, merging and breakup of clusters in the whole system as in the monodisperse case[31], leading to fluctuations in the maximum cluster size, as seen in Figs. 10 (a) and $10(c)$. Hence the maximum cluster size will show large fluctuations over a well-defined mean-value, and will always remain much less than the system size.

4.2   Pair correlation function

In order to connect our earlier observations on clustering with the microstructural informations at the particle-level, we present results on the pair correlation function, $g_{\alpha\beta}$. The effects of dissipation-levels and mass-disparity on $g_{\alpha\beta}$ are shown in Fig. 12. The parameter values are as in Fig. 8 except that restitution coefficients for the first and second columns are $e = 0.9$ and 0.5,

respectively. The crossed circle in each subplot represents the corresponding contact value for a homogeneous system (see Eq. B11). While the simulation data for the contact values of $g_{\alpha\beta}$, are rather well predicted by the theory at $e = 0.9$ and $R = 1$ as seen in Fig. 12(a), the theoretical predictions are well below the simulation results as we increase the dissipation levels as seen in Fig. 12(b). Another interesting feature is the emergence of a strong second peak with increasing dissipation as indicated by the respective arrow in each curve in Figs. 12(b) and 12(d). This is a consequence of the clustering process since the probablity of finding a second particle near the test particle increases as the mixture becomes more clustered with increasing dissipation.

Increasing the mass-ratio to $R_m = 16$, however, the peak values of both g_{ss} and g_{ls} are underpredicted and that of g_{ll} is overpredicted by the theory at $e = 0.9$ as seen from Fig. 12(c). Comparing subplots in the top row with those in the bottom row, we find that the effect of mass-disparity is to increase the contact values of g_{ss} and g_{ls} and decrease g_{ll}. This overall feature is consistent with the change in collision probabilities (as described in §2) and holds at other values of the size-ratio, e.g. at $R = 5$ as shown in Fig. 13. The decrease of g_{ll} with increasing R_m implies that the probability of finding a pair of two large particles is lower and hence the larger particles are better-mixed in an equal-density mixture as compared to an equal-mass mixture. This effect would, in turn, further increase the contact value of g_{ls}

as confirmed in these plots.

4.3   Collision angle distribution and the normal stress difference

We have monitored another measure of microstructural caveats, namely, the collision angle distribution function, $C_{\alpha\beta}(\theta)$, which is defined such that $C_{\alpha\beta}(\theta)d\theta$ is the probability that a collision between particles α and β occurs at an angle lying between $(\theta, \theta + d\theta)$, with θ being measured counterclockwise from the positive x-axis. This quantity provides information about the collisional anisotropy of the microstructure[30], and thereby links the microstructure with the first normal stress difference as we shall see below. For the uniform shear flow, it can be shown that $C_{\alpha\beta}(\theta)$ is directly proportional to the pair correlation function at contact [30, 36] and also depends on the volume fraction and the granular energy. In general, $C_{\alpha\beta}(\theta)$ is an anisotropic function of θ, depending on external driving.

Figure 14 shows the variations of $C_{\alpha\beta}(\theta)$ with θ for different values of the restitution coefficient for an equal-density mixture, with parameter values $\nu = 0.3$, $\chi = 0.5$ and $R = 4$. It is observed that the probability of collisions is higher on the *upstream-faces* (that contains the compression direction) of the colliding particles, i.e. for $\theta \in [\pi/2, \pi]$ and $\theta \in [-\pi/2, 0]$. This is simply a consequence of the imposed shear-field which compresses the flow-

structure along the $3\pi/4$-direction and stretches it along the $\pi/4$-direction as in Fig. 11. With increasing dissipation levels, the probability of collisions on the upstream faces increases and that on the downstream-faces decreases. Another noteworthy feature is that the position of the peak in each curve shifts towards lower values of θ with decreasing e, suggesting the possibility of more head-on collisions in the same limit. This implies that for a given mass-ratio the particle motion becomes more *streamlined* (i.e. *ordered* along the streamwise direction) with increasing dissipation level.

We note in Fig. 14(a) that the collision probability for the downstream faces (extensional direction) decreases with increasing dissipation and for the *ll*-collisions this practically vanishes for $e \leq 0.9$. This means that the larger species cannot communicate with each other anymore in this direction. Comparing Figs. 14(a) and 14(b), we find that the larger particles are more likely to collide on their upstream faces compared to the smaller particles at any dissipation level. This is presumably due to the fact that the smaller particles can move around much more freely than their larger counterparts since their fluctuating velocities are relatively higher. For example, the ratio of the mean-square fluctuation velocities, $< v_s^2 > / < v_l^2 >$, is 1.51, 2.38, 6.34 and 13.46 at $e = 0.5$, 0.7, 0.9 and 0.99, respectively.

The effect of mass-ratio on $C_{\alpha\beta}(\theta)$ is shown in Fig. 15 at a restitution coefficient of $e = 0.5$, with other parameter values as in Fig. 14. It is observed

that the collision probability between the smaller particles, C_{ss}, is little affected by changing R_m as in panel b, but that between the larger particles, C_{ll}, gets affected considerably as in panel a. In particular, C_{ll} becomes more asymmetric with increasing R_m in the sense that larger particles now collide more often on their upstream faces and their collisions on downstream faces become more rare. We observe in Fig. 15(c) that the collisions between large and small particles tend towards the regime of head-on collisions. This again implies that the particle motion becomes more *streamlined/ordered* with increasing mass-disparity. Thus, at a given dissipation-level, the effect of mass-disparity is to further enhance the *microscopic-ordering* of particles.

Now we relate our findings on the *microscopic-ordering* of particles with the behaviour of the first normal stress difference. We recall from §3.2 that it is the kinetic component of $\mathcal{N}_1$ which increases with increasing dissipation levels and mass-disparity (see also, Figs. 9 and 14 of Alam & Luding[20]). Hence we focus on the kinetic component of the stress tensor:

$$\mathbf{P}^k = \sum_{\alpha=l,s} < \rho_\alpha \mathbf{C}_\alpha \mathbf{C}_\alpha >,$$

where $\mathbf{C}_\alpha = (\mathbf{c}_\alpha - \mathbf{u})$ is the peculiar velocity of particles of species α, $\mathbf{c}_\alpha$ is its instantaneous velocity, and $\mathbf{u}$ is the mean velocity field. The kinetic component of the first normal stress difference $\mathcal{N}_1$ is

$$\mathcal{N}_1^k \sim [< \mathbf{C}_\alpha \mathbf{C}_\alpha >_x - < \mathbf{C}_\alpha \mathbf{C}_\alpha >_y]. \tag{18}$$

27

Associated with the microscopic-ordering of particles (along the streamwise direction) is an overall increase and decrease in the streamwise and transverse components of particle's fluctuating velocity, respectively. Hence $<\mathbf{C}_\alpha\mathbf{C}_\alpha>_x$ and $<\mathbf{C}_\alpha\mathbf{C}_\alpha>_y$ will increase and decrease, respectively, with increasing mass-ratio and dissipation. This clearly leads to an enhanced value of the first normal stress difference $\mathcal{N}_1$.

Thus, we can conclude that the *macroscopic* manifestation of *streamlined* (i.e. *ordered* along the streamwise direction) microscopic motion of particles is to increase and decrease the streamwise and transverse fluctuating velocities of the particles, respectively, leading to an increase in the magnitude of the first normal stress difference with increasing mass-disparity and dissipation.

Of course, such *microscopic-ordering* of particles is a clear signal of *short-range* correlations as well. It has recently been established, both via theory and simulation[30, 37, 38], that the effect of dissipation is to induce short-range correlations in a monodisperse granular fluid. Therefore, the present work suggests that the added effect of mass-disparity is to further enhance such short-range correlations in sheared bidisperse granular mixtures.

5 Summary and Conclusion

We have investigated the rheology and microstructure in a bidisperse granular mixture via event driven simulations in two-dimensions. The granular mixture is modelled as a collection of inelastic disks interacting via the hard-core potential. A generic feature of such mixtures is that the two species possess different levels of fluctuation kinetic energy ($T_l \neq T_s$) in contrast to their elastic counterpart [18, 19, 20, 21, 22, 23, 24, 25, 26, 27]. We have shown that the microscopic mechanism for this energy non-equipartition is directly tied to the *asymmetric* nature of collisional probabilities between the heavier and lighter species, compared to their purely elastic counterpart. The degree of this collisional asymmetry increases with both increasing inelasticity and mass-disparity, thereby increasing the energy ratio T_l/T_s in the same limit.

For the rheological study, we have looked at the effect of mass-disparity on the behaviour of transport coefficients in a bidisperse granular mixture in which the two species are of the same size but having different density. This complements our earlier work on the *equal mass* and *equal density* mixtures with different size particles[17, 20]. We reported results on *pressure*, *shear viscosity*, *granular energy* and *first normal stress difference* in a wide parameter space. A phenomenological constitutive model, allowing energy *non-equipartition*, is proposed which captures the non-monotonic behaviour of the transport coefficients, in agreement with simulation results, whereas the

standard constitutive model with equipartition assumption predicts *mono-tonic* variations. The reason for such non-monotonic behaviour is tied to the non-equipartition of granular energy. At large enough mass-ratios, the contributions of the lighter particles to the transport properties are very small because of their much smaller *fluctuation velocity* than the heavier species, and hence the mixture behaves like an effective lower-density system (composed only of the heavier particles).

In general, the bidisperse granular fluid is non-Newtonian with large normal stress differences as in the monodisperse case. The first normal stress difference increases with increasing both mass-disparity and dissipation. We have shown that, at the microscopic-level, the particle motion becomes more and more *streamlined* (i.e. *ordered-motion* along the streamwise direction) with increasing dissipation and mass-disparity. This clearly results in a decrease in the transverse component of the fluctuating velocity-field which, in turn, is responsible for the enhanced first normal stress difference. We have detected the microscopic-orderding of particles by monitoring the angular distribution of collisions between the colliding pair over the entire simulation time. Since such *ordered* particle-motion is also a signature of *short-range* correlations, we conclude that both the mass-disparity and the dissipation-level will enhance the *short-range* correlations in a sheared granular mixture.

The sheared granular mixture readily forms clusters, having striped-patterns

along the extensional-axis of the flow. This preferred orientation of clusters is simply due to the pure straining motion of the imposed shear field. We have extracted the microstructural flow-features by measuring the cluster-size distributions, the pair correlation function and the collision-angle distribution. The signature of clustering is tied to the emergence of a second peak in the pair-correlation function $g_{\alpha\beta}$ (refer to Figs. 12b and 12d) that becomes *stronger* with increasing dissipation levels.

While the inelastic dissipation is responsible for the onset of clustering, we have found that the mass-disparity between the two species enhances the degree of clustering. For example, the size of the largest cluster can increase by a factor of two or more if the particles are made of equal material density as compared to equal-mass particles for $e \leq 0.9$. This further suggests that the mass-disparity can be used as a manipulator to control the clustering process in a granular mixture. This issue needs further investigation in the future.

6   Acknowledgements

DFG and the AvH Foundation for support.

Appendix A: Details of simulations

For the hard-core potential, the collisions are instantaneous and the simulation moves in time from one collision to the next and so on. The pre- and post-collisional velocities of two colliding particles are related by the expression:

$$\mathbf{k}{\cdot}\tilde{\mathbf{c}}'_{ji} = -e_{ij}(\mathbf{k}{\cdot}\tilde{\mathbf{c}}_{ji}), \tag{A1}$$

where $\tilde{\mathbf{c}}_{ji} = \tilde{\mathbf{c}}_j - \tilde{\mathbf{c}}_i$ is the pre-collisional velocity of particle j relative to i ($\tilde{\mathbf{c}}'_{ji}$ being the corresponding post-collisional relative velocity), $\mathbf{k}_{ji} = \mathbf{k}$ the unit vector directed from the center of the particle j to that of particle i, and e_{ij} is the coefficient of normal restitution for collisions between particle i and j, with $e_{ij} = e_{ji}$ and $0 \leq e_{ij} \leq 1$. We used $e = e_{ij}$ for all simulations. The expression for the collisional impulse is

$$\tilde{\mathbf{I}}_{ij} \;=\; \tilde{m}_i(\tilde{\mathbf{c}}'_i - \tilde{\mathbf{c}}_i) \;=\; \tilde{m}_i M_{ji}(1 + e_{ji})(\mathbf{k}{\cdot}\tilde{\mathbf{c}}_{ji})\mathbf{k}, \tag{A2}$$

where $M_{ij} = \tilde{m}_i/(\tilde{m}_i + \tilde{m}_j)$. We drive a collection of smooth inelastic hard-disks (with d_i and m_i being the diameter and mass of species i) in a square box of size $\tilde{L}$ by the uniform shear flow, using the Lees-Edwards boundary condition[28, 39]. This represents an *extended doubly-periodic* system where the periodicity in the transverse direction is in the local Lagrangian frame. Let $\tilde{x}$ and $\tilde{y}$ be the streamwise and transverse directions, respectively, with the origin of the coordinate-frame being positioned at the centre of the box.

The macroscopic stress and the related transport coefficients (pressure, shear viscosity, and the normal stress differences) are calculated from the simulation data. For the uniform shear flow (with the overall shear rate $\tilde{\gamma}$), all these quantities (except the streamwise velocity which varies linearly with the transverse coordinate) are uniform in the computational box, and hence the averaging is done over all the particles. Defining $\tilde{L}$, $\tilde{\gamma}^{-1}$ and $\tilde{\gamma}\tilde{L}$ as the reference scales for length, time, velocity and mass, respectively, the relevant dimensionless variables are:

$$d_\alpha = \frac{\tilde{d}_\alpha}{\tilde{L}}, \quad (\mathbf{c}_\alpha, \mathbf{u}, \mathbf{C}_\alpha) = \frac{1}{\tilde{\gamma}\tilde{L}}(\tilde{\mathbf{c}}_\alpha, \tilde{\mathbf{u}}, \tilde{\mathbf{C}}_\alpha), \tag{A3}$$

where $\tilde{\mathbf{u}}$ is the mass-averaged velocity, $\tilde{\mathbf{C}}_\alpha = \tilde{\mathbf{c}}_\alpha - \tilde{\mathbf{u}}$ the peculiar velocity of particles of species α. As in our previous work [20], the total stress and the mixture granular energy are rescaled by the species-averaged momemtum flux density and kinetic energy, respectively:

$$\mathbf{P} = \frac{\tilde{\mathbf{P}}}{\tilde{\gamma}^2 \sum_{\alpha=l,s} \chi_\alpha \tilde{\rho}_\alpha \tilde{d}_\alpha^2}, \quad T = \frac{\tilde{T}}{\tilde{\gamma}^2 \sum_{\alpha=l,s} \chi_\alpha \tilde{m}_\alpha \tilde{d}_\alpha^2}, \tag{A4}$$

where $\chi_\alpha = \nu_\alpha/\nu$ is the relative volume fraction of species α.

The 'time-averaged' bulk stress, in non-dimensional form, is calculated from

$$
\begin{aligned}
\mathbf{P} &= \sum_{\alpha=l,s} (\mathbf{P}_\alpha^k + \mathbf{P}_\alpha^c) \\
&= \sum_{\alpha=l,s} \frac{\pi}{4 \sum_{\beta=l,s} \frac{\rho_\beta}{\rho_l} \chi_\beta R_{\beta l}^2} \left[m_\alpha \sum_{i=1}^{N_\alpha} \mathbf{C}_i \otimes \mathbf{C}_i + \frac{1}{2\tau_d} \sum_{collisions} (d_i + d_j)(\mathbf{I}_{ij} \otimes \mathbf{k}) \right] \tag{A5}
\end{aligned}
$$

where $\mathbf{P}_\alpha^k$ and $\mathbf{P}_\alpha^c$ are the kinetic and collisional contributions to the partial stress $\mathbf{P}_\alpha$, respectively. Note that for the collisional component of the bulk stress the sum is taken over all collisions during the averaging time window τ_d. In the above equation, the sum over the index β in the denominator is due to our adopted scaling (A4), and $R_{\beta l} = d_\beta/d_l$ is the size ratio. Now we decompose the total stress, defined in the *compressive* sense, in the following way:

$$\mathbf{P} = \sum_{\alpha=l,s}(\mathbf{P}_\alpha^k + \mathbf{P}_\alpha^c) = p\mathbf{1} + \mathbf{\Pi}, \qquad (A6)$$

where p is the pressure, $\mathbf{\Pi}$ the pressure deviator and $\mathbf{1}$ the unit tensor. The off-diagonal components of the pressure deviator can be related to the *shear viscosity* via

$$\mu = -\Pi_{xy}\left/\frac{\mathrm{d}u}{\mathrm{d}y}\right., \qquad (A7)$$

where u is the streamwise velocity. Note that this is the effective viscosity of the granular mixture which is defined as the ratio of the (x,y)-component of the bulk stress to the shear rate[5, 40]. The diagonal components of the pressure deviator could be different from zero, giving rise to the *first normal stress difference*, defined as:

$$\mathcal{N}_1 = \frac{(\Pi_{xx} - \Pi_{yy})}{p}. \qquad (A8)$$

Note that this is not the standard definition of the first normal stress difference since we have scaled this quantity by pressure which, in turn, helps

to discern its relative magnitude with respect to pressure. For a standard Newtonian fluid, $\mathcal{N}_1 = 0$ and thus $\mathcal{N}_1$ is an indicator of the *non-Newtonian* character of the fluid.

The *species* granular energy is calculated from the following expression:

$$T_\alpha = \frac{1}{2d_l^2 \sum_{\beta=l,s} \frac{m_\beta}{m_l} \chi_\beta R_{\beta l}^2} \left[\frac{m_\alpha}{N_\alpha} \sum_{i=1}^{N_\alpha} \mathbf{C}_i \cdot \mathbf{C}_i \right] \tag{A9}$$

The total granular energy is $T = \sum_{\alpha=l,s} \xi_\alpha T_\alpha$, where $\xi_\alpha = N_\alpha/N$ is the number fraction of species α. Note that the granular energy may be obtained from the trace of the kinetic part of the stress tensor.

The disks are initially placed randomly in the central box, and the initial velocity field is composed of the uniform shear and a small Gaussian random part. An event-driven algorithm[28, 29] is then used to simulate instantaneous binary collisions[17, 20, 30]. At the steady state, the uniform shear flow attains a constant granular energy due to the balance between the shear work and the collisional dissipation (see Fig. 1). After reaching this steady-state, the simulation was allowed to run for at least another 4000 collisions per particle to gather data to calculate the rheological and microstructural quantities. The total number of particles was varied between 1024 and 5100. The simulations are carried out for the coefficient of restitution $e > 0.2$ and upto a maximum mass ratio R_m of 100. For the range of parameters studied, we found that the system-size dependence[20, 32] of the rheological quantities is negligible if $N > 500$ as in our earlier study[20].

Appendix B: A phenomenological constitutive model for inelastic disks

The balance equations for a binary granular mixture and the corresponding constitutive relations[16, 17], with equipartition assumption, are documented in our previous paper[20]. Here we incoporate the breakdown of energy nonequipartition in these constitutive expressions in a phenomenological way. Assuming that the single particle distribution function of species α is a Maxwellian at the species granular energy T_α, an expression for the collisional dissipation rate of hard-disks can be obtained as[18]:

$$
\tilde{\mathcal{D}} = \sum_{\alpha=l,s} \tilde{\mathcal{D}}_\alpha = \sum_{\alpha=l,s} \sum_{\beta=l,s} \sqrt{2\pi} \tilde{m}_\alpha \tilde{n}_\alpha \tilde{n}_\beta g_{\alpha\beta} \tilde{d}_{\alpha\beta} M_{\beta\alpha}^2 (1 - e_{\alpha\beta}^2) \left(\frac{\tilde{T}_\alpha}{\tilde{m}_\alpha} + \frac{\tilde{T}_\beta}{\tilde{m}_\beta} \right)^{3/2} \tag{B1}
$$

$$
= \frac{\sqrt{\tilde{\rho}_l}}{\tilde{m}_l \tilde{d}_l^2} \sum_{\alpha=l,s} f_{5\alpha} \tilde{T}_\alpha^{3/2} R_{l\alpha}^2 \frac{m_l}{m_\alpha} \sqrt{\frac{\rho_\alpha}{\rho_l}} , \tag{B2}
$$

where $\tilde{d}_{\alpha\beta} = (\tilde{d}_\alpha + \tilde{d}_\beta)/2$, $R_{l\alpha} = \tilde{d}_l/\tilde{d}_\alpha$, $M_{\beta\alpha} = \tilde{m}_\beta/(\tilde{m}_\alpha + \tilde{m}_\beta)$ and $f_{5\alpha}$ is a non-dimensional function of the form:

$$
f_{5\alpha} = \frac{4\sqrt{2}\nu_\alpha}{\pi} \sum_{\beta=l,s} \nu_\beta g_{\alpha\beta}(1 + R_{\beta\alpha}) R_{\alpha\beta}^2 (1 - e_{\alpha\beta}^2) M_{\beta\alpha}^2 \left(1 + \frac{m_\alpha}{m_\beta} \frac{T_\beta}{T_\alpha} \right)^{3/2} . \tag{B3}
$$

The constitutive relation (B.1) is exactly equal to that of Willits and Aranson[16]:

$$
\tilde{\mathcal{D}} = \sum_{\alpha=l,s} \sum_{\beta=l,s} \tilde{n}_\alpha \tilde{n}_\beta g_{\alpha\beta} \tilde{d}_{\alpha\beta} M_{\beta\alpha} (1 - e_{\alpha\beta}^2) \left(\frac{2\pi \tilde{T}^3}{\tilde{m}_\alpha M_{\beta\alpha}} \right)^{1/2} , \tag{B4}
$$

with the equipartition assumption, $T_\alpha = T_\beta$. Note further that the exact expression (B.1) can be obtained from eqn. (B.4) by simply replacing T with

$(m_\alpha^{-1}T_\alpha + m_\beta^{-1}T_\beta)/(m_\alpha^{-1} + m_\beta^{-1})$. This can be thought of as modifying the inter-species collision rates for two species.

The total stress tensor, $\tilde{\mathbf{P}}$, is of the standard Newtonian form:

$$\tilde{\mathbf{P}} = \tilde{p}\mathbf{1} - 2\tilde{\mu}\tilde{\mathbf{S}}, \tag{B5}$$

where p is the pressure, μ the shear viscosity, and $\tilde{\lambda} = \tilde{\zeta} - 2\tilde{\mu}/3$, with $\tilde{\zeta}$ being the bulk viscosity; the rate of shear tensor (*i.e.*, the deviatoric part of the deformation tensor), $\tilde{\mathbf{S}}$, is given by

$$\tilde{\mathbf{S}} = \frac{1}{2}\left(\tilde{\nabla}\tilde{\mathbf{u}} + \tilde{\nabla}\tilde{\mathbf{u}}^T\right) - \frac{1}{2}(\tilde{\nabla} \cdot \tilde{\mathbf{u}}).$$

Following the expression of the collisional dissipation rate in eqn (B.1), the constitutive expressions for p and μ (as detailed in ref. [20]) are modified to have following forms:

$$\tilde{p} = \frac{4}{\pi}\tilde{d}_l^{-2}\sum_{\alpha=l,s}f_{1\alpha}\tilde{T}_\alpha, \tag{B6}$$

$$\tilde{\mu} = \sqrt{\tilde{\rho}_l}\sum_{\alpha=l,s}f_{2\alpha}\tilde{T}_\alpha^{1/2}\sqrt{\frac{\rho_\alpha}{\rho_l}}, \tag{B7}$$

where the non-dimensional functions $f_{1\alpha}$ and $f_{2\alpha}$ are given by

$$f_{1\alpha} = \nu_\alpha R_{l\alpha}^2\sum_{\beta=l,s}\left[1 + \frac{1}{4}(1+e_{\alpha\beta})(1+R_{\alpha\beta})^2\nu_\beta g_{\alpha\beta}M_{\beta\alpha}\left(1 + \frac{m_\alpha}{m_\beta}\frac{T_\beta}{T_\alpha}\right)\right] \tag{B8}$$

$$f_{2\alpha} = \frac{\overline{b}_{\alpha 0}}{2}\sum_{\beta=l,s}\left[1 + \frac{1}{2}\nu_\beta g_{\alpha\beta}(1+R_{\alpha\beta})^2 M_{\beta\alpha}^{3/2}\left(1 + \frac{m_\alpha}{m_\beta}\frac{T_\beta}{T_\alpha}\right)^{1/2}\right]$$

$$+ \frac{\nu_\alpha}{2\sqrt{2\pi}}\sum_{\beta=l}^s\nu_\beta g_{\alpha\beta}R_{\beta\alpha}(1+R_{\alpha\beta})^3 M_{\beta\alpha}\left(1 + \frac{m_\alpha}{m_\beta}\frac{T_\beta}{T_\alpha}\right)^{1/2}, \tag{B9}$$

38

with

$$\bar{b}_{\alpha 0} = \frac{\sqrt{M_{k\alpha}}}{\sqrt{2}(1+R_{k\alpha})g_{\alpha k}} \left[\frac{(\nu_\alpha/\nu_k)R_{k\alpha}^2 K'_\alpha B_\alpha + K'_k M_{\alpha k} M_{k\alpha}}{B_\alpha B_k - M_{\alpha k}^2 M_{k\alpha}^2} \right]$$

$$B_\alpha = M_{\alpha k}(M_{\alpha k} + 2M_{k\alpha}) + \frac{R_{\alpha k}^2}{(1+R_{\alpha k})} \frac{\nu_k}{\nu_\alpha} \frac{g_{kk}}{g_{\alpha k}} \left(\frac{M_{\alpha k}}{M_{kk}} \right)^{1/2}$$

$$K'_\alpha = 1 + \tfrac{1}{2} \sum_{\beta=l,s} \nu_\beta (1+R_{\alpha\beta})^2 g_{\alpha\beta} M_{\beta\alpha},$$

with $k \neq \alpha$. The functional form of $f_{1\alpha}$ can be understood by decomposing the total pressure into its kinetic and collisional contributions:

$$\tilde{p} = \tilde{p}^k + \tilde{p}^c.$$

Again with the assumption of an Maxwellian distribution function (at species granular energy), an expression for the kinetic part of the pressure can obtained as

$$\tilde{p}^k = \sum_{\alpha=l,s} \tilde{p}_\alpha^k = \sum_{\alpha=l,s} \tilde{n}_\alpha \tilde{T}_\alpha = \sum_{\alpha=l,s} \frac{4}{\pi} \tilde{d}_\alpha^{-2} \nu_\alpha \tilde{T}_\alpha = \frac{4}{\pi} \tilde{d}_l^{-2} \sum_{\alpha=l,s} R_{l\alpha}^2 \nu_\alpha \tilde{T}_\alpha. \quad \text{(B10)}$$

This is the first term within the square-bracket in eqn (B.8). The corresponding collisional contributions to both $f_{1\alpha}$ and $f_{2\alpha}$ are simply obtained by modifying the original expressions in ref. [16, 17] by following the exact expression for $\mathcal{D}$ in eqn. (B.1). With the equipartition assumption, the expressions for $f_{1\alpha}$ and $f_{2\alpha}$ boil down to those in [16, 17].

The radial distribution function at contact $g_{\alpha\beta}$ is taken as that of Mansoori et $al.$[41] for disks:

$$g_{\alpha\beta} = \frac{1}{(1-\nu)} + \frac{9}{8} \frac{(\nu_l R_{\alpha l} + \nu_s R_{\alpha s})}{(1+R_{\alpha\beta})(1-\nu)^2}. \quad \text{(B11)}$$

Note that $g_{\alpha\beta}$ should diverge in the close packing limit ($\nu = \nu_{max}$), (rather than at $\nu \to 1$) which corresponds to $\nu_{max} = \pi/2\sqrt{3} \approx 0.9069$ for a monodisperse system with triangular packing; for a bidisperse system, ν_{max} is also a function of the mass and size ratios[22]. A better choice for the radial distribution function does not, however, influence the theoretical predictions for pressure and viscosity if $\nu \leq 0.55$. Corrections to Eq. (B11), as reported by Luding & Santos[42], are disregarded here since they are mostly less than one percent.

The granular energy ratio, $R_T = T_l/T_s$, is calculated from the relation given by Barrat & Trizac[25]:

$$a_1 R_T^{3/2} + a_2 \left(1 + \frac{m_s}{m_l} R_T\right)^{3/2} + a_3 \left(1 + \frac{m_s}{m_l} R_T\right)^{1/2} (R_T - 1) + a_4 = 0, \quad \text{(B12)}$$

where the non-dimensional functions a_i are

$$a_1 = 2(1 - e_{ll}^2)\nu_l R_{sl}^2 g_{ll} \left(\frac{m_s}{m_l}\right)^{3/2}$$

$$a_2 = \sqrt{2}(1 - e_{ls}^2)(1 + R_{sl}) \left(\nu_s M_{sl}^2 - \nu_l R_{sl}^2 M_{ls}^2\right) g_{ls}$$

$$a_3 = 2\sqrt{2}(1 + e_{ls})(1 + R_{sl}) M_{sl} \left(\nu_s M_{sl} + \nu_l R_{sl}^2 M_{ls}\right) g_{ls}$$

$$a_4 = -2(1 - e_{ss}^2)\nu_s R_{sl} g_{ss}.$$

Even though this model is based on the assumption of a randomly (homogeneous) excited granular mixture, it provides good agreement with the MD simulation results of a sheared granular mixture[19].

References

[1] H.J. Herrmann, J.-P. Hovi and S. Luding, *Physics of Dry Granular Media*, NATO ASI Series E 350 (Kluwer Academic, Dordrecht, 1998).

[2] T. Pöschel and S. Luding, *Granular Gases*, Lecture Notes in Physics 764 (Springer Verlag, Berlin, 2001).

[3] C.S. Campbell, "Rapid granular flows," Annu. Rev. Fluid Mech. **22**, 57 (1990).

[4] I. Goldhirsch, "Rapid granular flows," Annu. Rev. Fluid Mech. **35**, 267 (2003).

[5] J.F. Brady and G. Bossis, "Stokesian Dynamics," Annu. Rev. Fluid Mech. **20**, 111 (1988).

[6] H.M. Jaeger, S.R. Nagel and R. P. Behringer, "Granular solids, liquids and gases," Rev. Mod. Phys. **68**, 1259 (1996).

[7] A.D. Rosato, K.J. Strandburg, F. Prinz and R.H. Swendsen, "Why the Brazil nuts are on top: size segregation of particulate matter by shaking," Phys. Rev. Lett. **58**, 1038 (1987).

[8] D.V. Khakhar, J. McCarthy, T. Shinbrot and J.M. Ottino, "Mixing and segregation of granular materials," Phys. Fluids **9**, 31 (1999).

41

[9] S. Luding, O. Strauss and S. McNamara, "Segregation of polydisperse granular media in the presence of a temperature gradient," in: Segregation in Granular Flows, T. Rosato (Ed.), Proceedings of the IUTAM Symposium, pp. 189-195. (Kluwer Academic, Dordrecht, 2000).

[10] L. Trujillo, M. Alam and H.J. Herrmann, "Segregation in a fluidized binary granular mixture: Competition between buoyancy and geometric forces," Europhys. Lett. **64**, 190 (2003).

[11] S. Chapman and T.G. Cowling, *The Mathematical Theory of Nonuniform Gases* (Cambridge University Press, Cambridge, 1970).

[12] J. Ferziger and H. Kaper, *Mathematical Theory of Transport Processes in Gases* (North-Holland, Amsterdam, 1972).

[13] M. López de Haro, E.G.D. Cohen and J.M. Kincaid, "The Enskog theory for multicomponent mixtures. I. Linear transport theory," J. Chem. Phys. **78**, 2746 (1983).

[14] J. Jenkin and F. Mancini, "Kinetic theory for binary mixtures of smooth, nearly elastic spheres," Phys. Fluids **A 1**, 2050 (1989).

[15] P. Zamankhan, "Kinetic theory for multicomponent dense mixtures of slightly inelastic spherical grains," Phys. Rev. E **52**, 4877 (1995).

[16] J.T. Willits and B.Ö. Arnarson, "Kinetic theory for a binary mixture of smooth elastic disks," Phys. Fluids **11**, 3116 (1999).

[17] M. Alam, J. Willits, B. Arnarson, and S. Luding, "Kinetic theory for binary mixtures of smooth nearly elastic disks with size and mass disparity," Phys. Fluids **14**(11), 4085 (2002).

[18] V. Garzó and J.W. Dufty, "Homogeneous cooling state for a granular mixture," Phys. Rev. E **60**, 5706 (1999).

[19] M. Alam and S. Luding, "How good is the equipartition assumption for the transport properties of a granular mixture?" Granular Matter **4**, 139 (2002).

[20] M. Alam and S. Luding, "Rheology of bidisperse granular mixtures via event-driven simulations," J. Fluid Mech. **476**, 69 (2003).

[21] W. Losert, D. Cooper, J. Delour, A. Kudrolli and J.P. Gollub, "Velocity statistics in excited granular media," Chaos **9**(3), 682 (1999).

[22] S. Luding and O. Strauss, "The equation of state of polydisperse granular gases," in: Granular gases, T. Pöschel, S. Luding, (Eds.), Lecture Notes in Physics 564, Springer Verlag, Berlin, pp. 389-409 (2001).

[23] J.M. Montanero and V. Garzó, "Monte carlo simulation of the homogeneous cooling state for a granular mixture," Granular Matter **4**, 17 (2002).

[24] R. Cleland and C. Herenya, "Simulations of a sized mixture of inelastic disks in rapid shear flow," Phys. Rev. E **65**, 031301 (2002).

[25] A. Barrat and E. Trizac, "Lack of energy equipartition in homogeneous heated binary granular mixtures," Granular Matter **4**, 57 (2002).

[26] R. Wildman and D. Parker, "Coexistence of two granular temperatures in binary vibrofluidzed beds," Phys. Rev. Lett. **88**, 064301 (2002).

[27] K. Feitosa and N. Menon, "Breakdown of energy equipartition in a 2D binary vibrated granular gas," Phys. Rev. Lett. **88**, 198301 (2002).

[28] M.P. Allen and D.J. Tildesley, *Computer Simulation of Liquids* (Oxford University Press, New York, 1989)

[29] D. C. Rapaport, *The Art of Molecular Dynamics Simulation* (Cambridge University Press, Cambridge, 1995)

[30] M. Alam and S. Luding, "First normal stress difference and crystallization in a dense sheared granular fluid," Phys. Fluids **15**, 2298 (2003).

[31] M. Tan and I. Goldhirsch, "Intercluster interactions in rapid granular shear flows," Phys. Fluids **9**, 856 (1997).

[32] E. Liss and B.J. Glasser, "The influence of clusters on the stress in a sheared granular material," Powder Tech. **116**, 116 (2001).

[33] M. Hopkins and M.Y. Louge, "Inelastic microstructure in rapid granular flows of smooth disks," Phys. Fluids **A 3**, 47 (1991).

[34] S. Luding and H.J. Herrmann, "Cluster growth in freely cooling granular media," Chaos **9**, 673 (1999).

[35] S. Luding and S. McNamara, "How to handle the inelastic collapse of a dissipative hard-sphere gas with the TC model," Granular Matter **1**, 113 (1998).

[36] C.S. Campbell and C.E. Brennen, "Computer simulation of granular shear flows," J. Fluid Mech. **151**, 167 (1985).

[37] R. Soto, M. Piasecki and M. Mareschal, "Statistical mechanics of fluidized granular media: short range velocity correlations," Phys. Rev. E **64**, 031306 (2001).

[38] J.F. Lutsko, "Atomic-scale structure of hard-core fluids under shear flow," Phys. Rev. E **66**, 051109 (2002).

[39] A.W. Lees and S.F. Edwards, "The computer study of transport processes under extreme conditions," J. Phys. C **5**(6):2746 (1972).

[40] J.F. Brady and M. Vicic, "Normal stresses in colloidal dispersions," J. Rheol. **39**, 545 (1995).

[41] G.A. Mansoori, N.F. Carnahan, K.E. Starling and T.W. Leland, "Equilibrium thermodynamics properties of the mixture of hard spheres," J. Chem. Phys. **54**, 1523 (1971).

[42] S. Luding and A. Santos, "Molecular dynamics and theory for the contact values of the radial distribution functions of hard-disk fluid mixtures," J. Chem. Phys. **121** (17), 8458 (2004).

LIST OF FIGURE CAPTIONS

FIG. 1. Variations of species granular energies, T_l and T_s, with time for $\nu = 0.05$, $\chi = 0.5$, $e = 0.9$, $R = 1$, $R^m = 9$ and $N = 1024$. The inset shows the temporal variation of the granular energy ratio $R_T = T_l/T_s$.

FIG. 2. Variations of collision probabilities with the mass-ratio for $\nu = 0.05$, $\chi = 0.5$ and $R = 1$ at a restitution coefficient of $e = 0.9$. The lines are drawn to guide the eye. The inset shows the variation of effective collision probability, Ω_α, with R_m.

FIG. 3. Variation of the effective collision ratio, R_Ω, with the mass-ratio; parameter values as in Fig. 2. The inset shows the variation of the energy ratio, $R_T = T_l/T_s$, with R_m. The lines are drawn to guide the eye.

FIG. 4. Variations of (a) pressure, (b) viscosity and their partial components, with the mass-ratio $R_m = m_l/m_s$ for a mixture of equal-size particles ($R = d_l/d_s = 1$) with $\nu = 0.01$, $\chi = 0.5$ and $e = 0.9$. Symbols denote simulation data and the lines the model predictions. (c) Comparison of granular energy between simulation and theory: solid line is the model prediction, T^{ne}, with non-equipartition of energy, and the dashed line, T^e, with equipartition assumption. The inset shows the granular energy ratio and its comparison

with theory [25].

FIG. 5. Variations of (a, c) pressure, (b, d) viscosity and their partial components, with the volume fraction ν at $R = 1$, $\chi = 0.5$ and $e = 0.9$; $(a$-$b)$ $R_m = 9$, $(c$-$d)$ $R_m = 25$. Symbols denote simulation data and the lines the model predictions.

FIG. 6. Same as Fig. 4, but at a moderate solid fraction $(\nu = 0.3)$ with *different size* particles $R = d_l/d_s = 2$.

FIG. 7. Variations of the first normal stress difference, $\mathcal{N}_1$, with (a) the mass-ratio at $\nu = 0.3$, and (b) the volume fraction at $e = 0.9$; $\chi = 0.5$ and $R = 1$ for both subplots. The lines are here merely a guide to the eye.

FIG. 8. Effects of dissipation and mass-ratio on *clustering* in a bidisperse sheared granular fluid: $\nu = 0.3$, $\chi = 0.5$ and $R = 4$. For panels on the top-row, the mixture is of equal-density particles (i.e. $R_m = 16$), and for the bottom-row $R_m = 1$. The coefficient of restitution is (a, c) $e = 0.99$; (b, d) $e = 0.5$.

FIG. 9. Maps of fluctuating solid fraction, $\nu'(x, y) = \nu(x, y) - \nu_{av}$, after

1.5×10^7 collisions: $\nu = 0.3$, $\chi = 0.5$, $R = 4$ and $e = 0.5$. (a) $R_m = 16.0$ and (b) $R_m = 1.0$. On the grey-scale, black represents maximum solid fraction and white maximum; $\nu'(x, y)$ varies from -0.3 to 0.4 in these plots.

FIG. 10. Variations of mean and maximum cluster sizes: $\nu = 0.3$, $\chi = 0.5$ and $R = 4$. For an equal-density mixture: (a) time evolution of $< M >$ and M_{max} at $e = 0.5$; (b) variations of the time-averaged $< M >$ and M_{max} with the coefficient of restitution. For an equal-mass mixture: (c) time evolution of $< M >$ and M_{max} at $e = 0.5$; (d) variations of the time-averaged $< M >$ and M_{max} with the coefficient of restitution.

FIG. 11. An sketch of streamline patterns for pure rotation and pure straining motion of the uniform shear flow.

FIG. 12. Effects of dissipation and mass-disparity on the pair correlation function: $\nu = 0.3$, $\chi = 0.5$ and $R = 4$. (a) $e = 0.9$, $R_m = 1$; (b) $e = 0.5$, $R_m = 1$; (c) $e = 0.9$, $R_m = 16$; (d) $e = 0.5$, $R_m = 16$.

FIG. 13. Effect of mass-disparity on the pair correlation function at a size ratio $R = 5$: (a) $R_m = 1$; (b) $R_m = 25$. The coefficient of restitution is $e = 0.5$ and other parameters are as in Fig. 12.

FIG. 14. Effect of dissipation-levels on the collision angle distribution for an equal-density mixture: $\nu = 0.3$, $\chi = 0.5$, $R = 4$ and $R_m = 16$.

FIG. 15. Effect of mass-disparity on the collision angle distribution: $\nu = 0.3$, $\chi = 0.5$, $R = 4$ and $e = 0.5$.
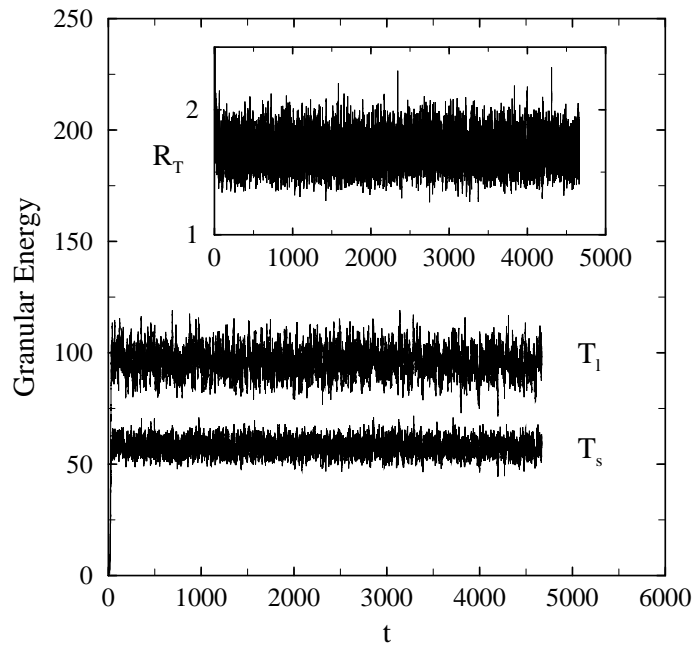
Figure 1, Alam, Physics of Fluids
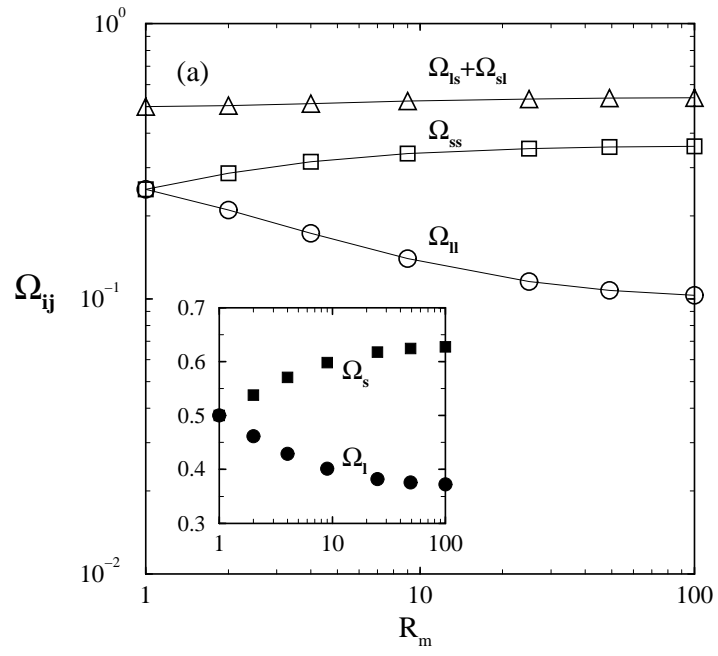
Figure 2, Alam, Physics of Fluids

1
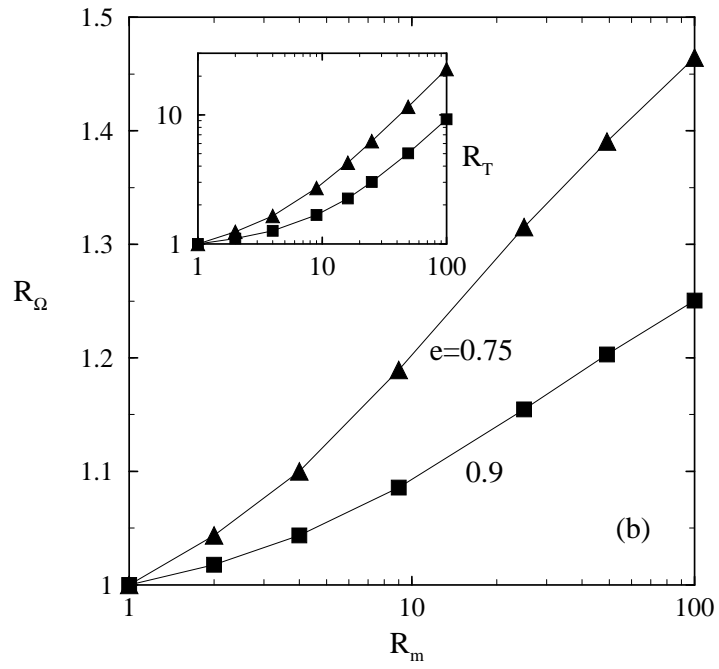
Figure 3, Alam, Physics of Fluids
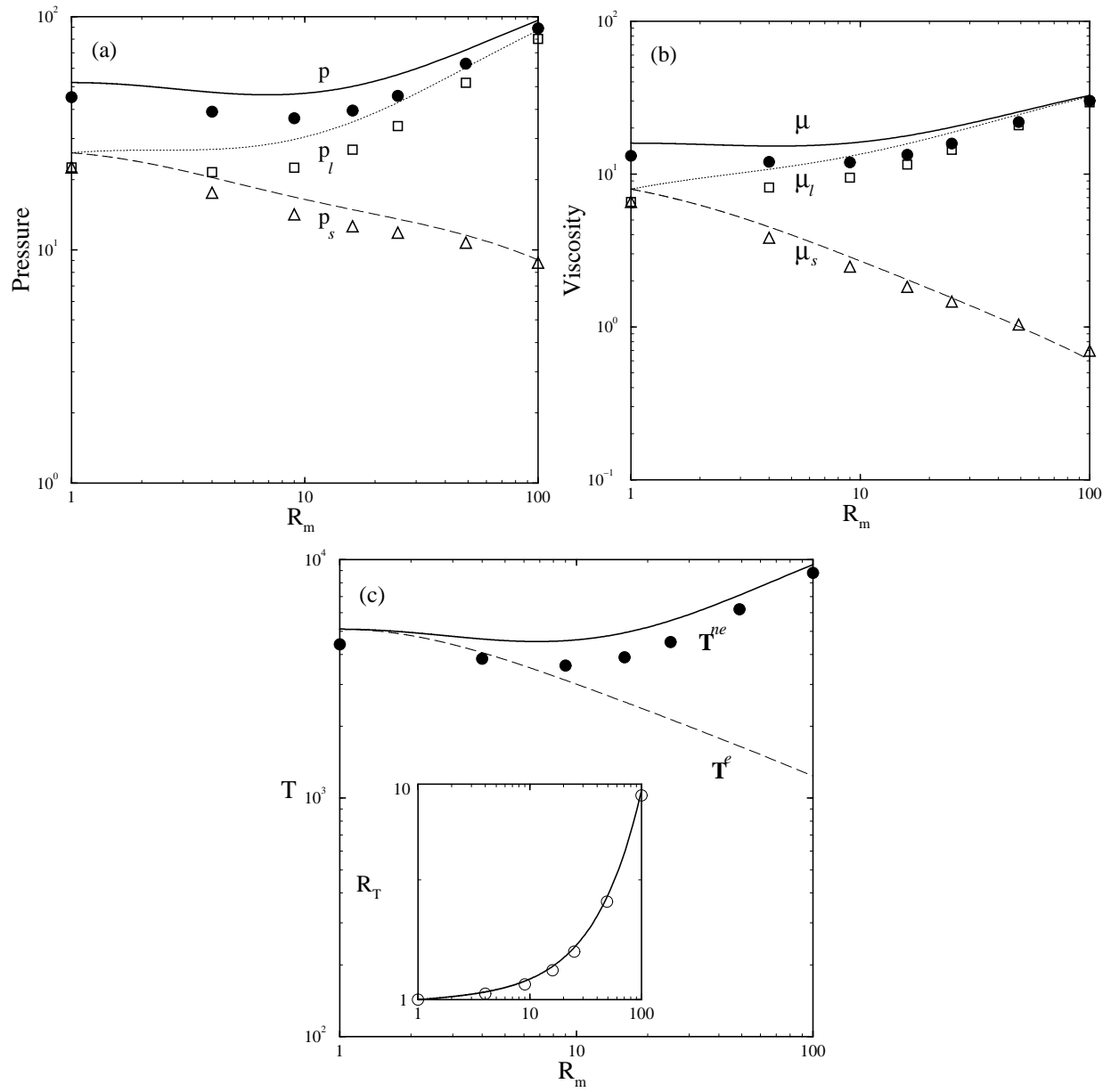
Figure 4, Alam, Physics of Fluids

1
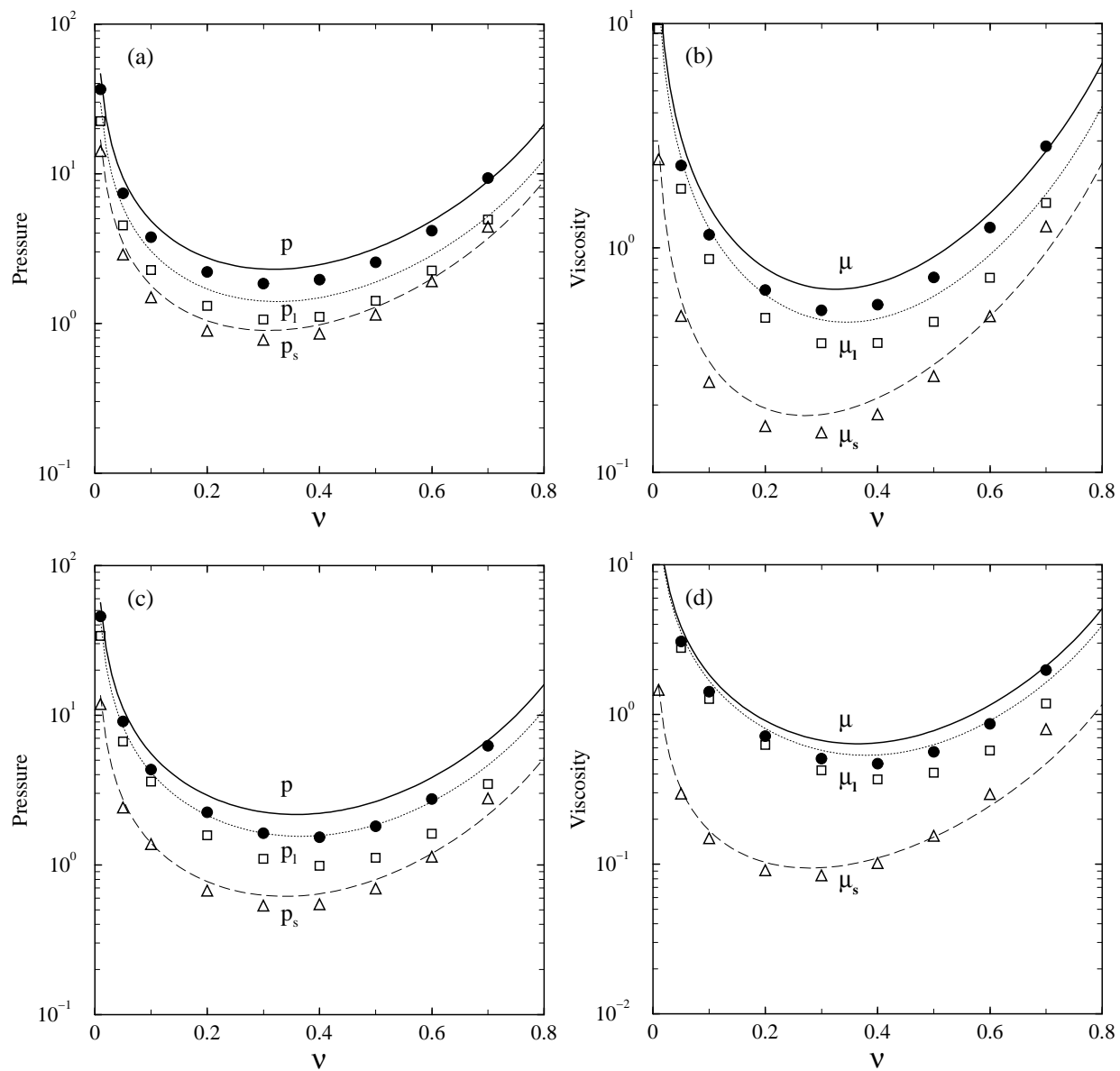
Figure 5, Alam, Physics of Fluids

1
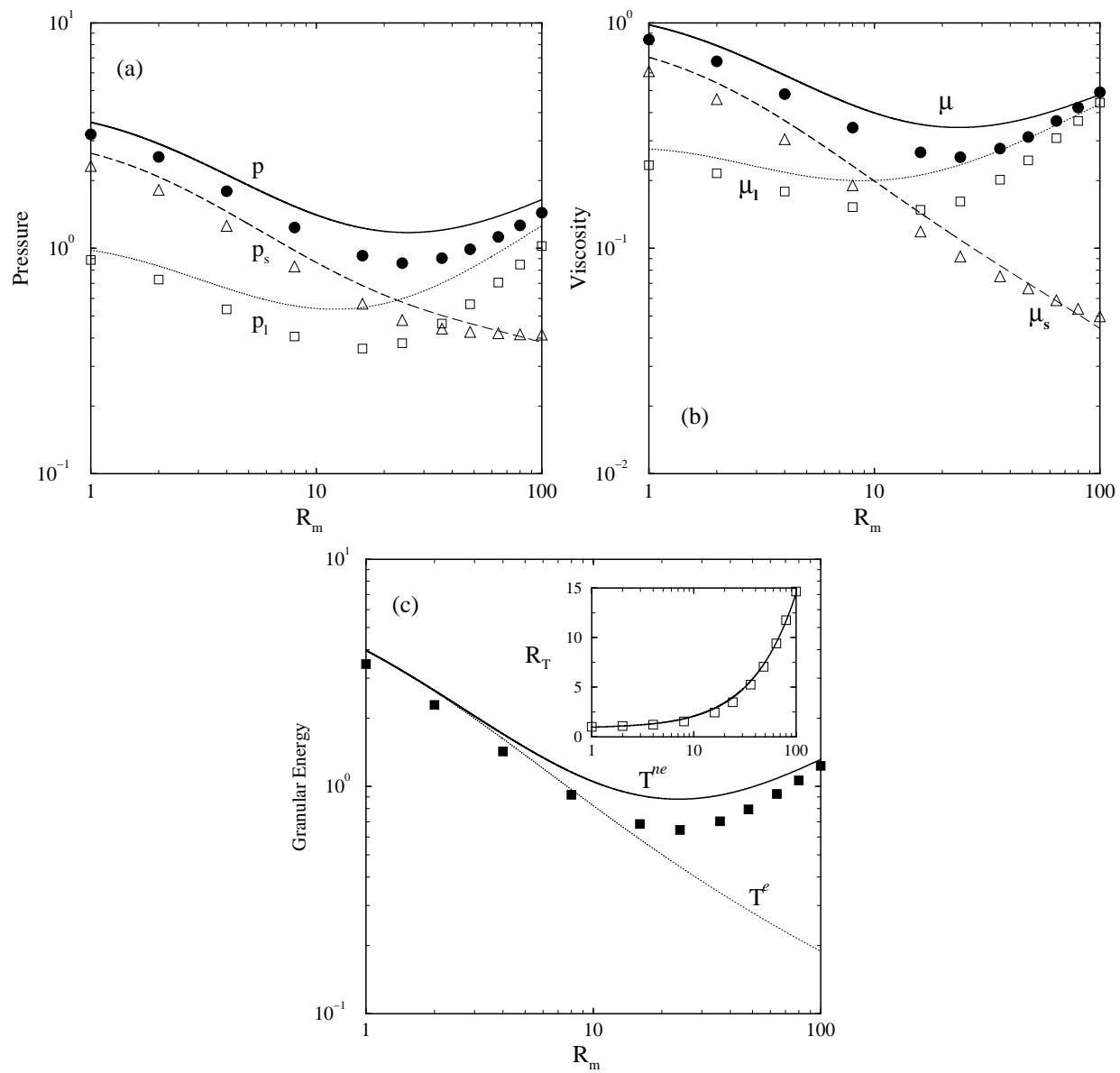
Figure 6, Alam, Physics of Fluids
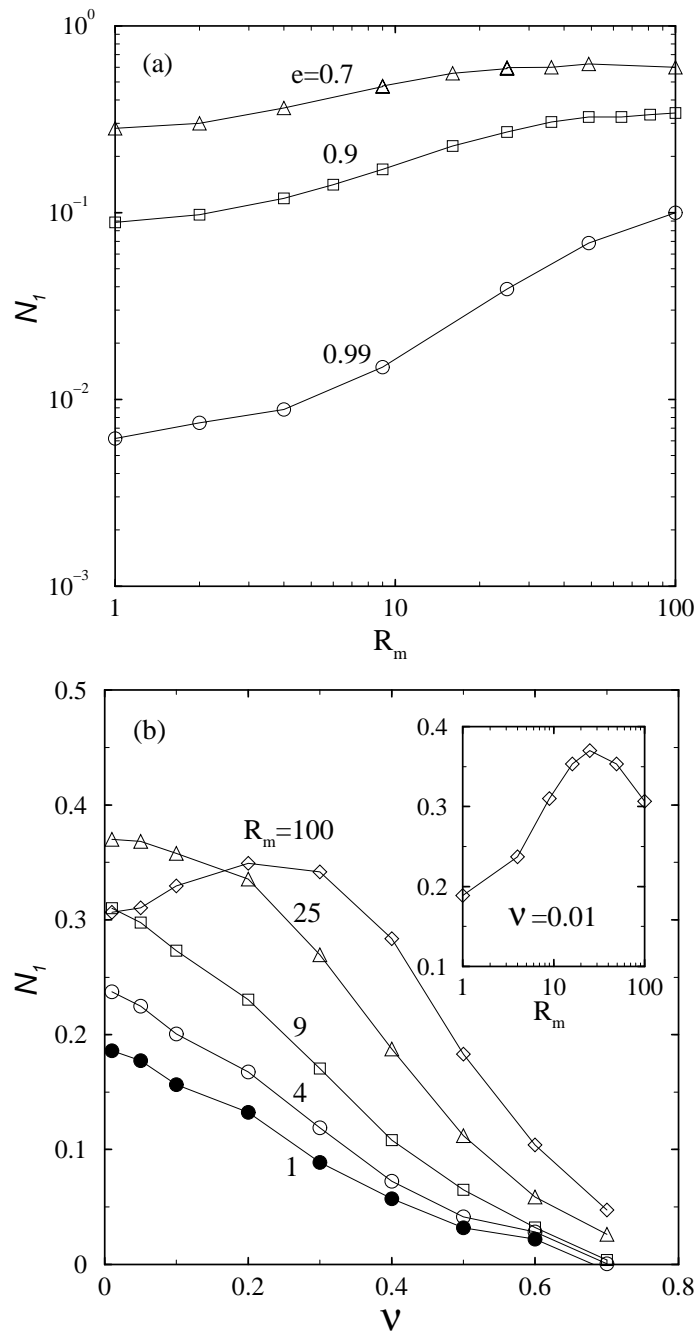
Figure 7, Alam, Physics of Fluids

(a)

(b)

(c)

(d)
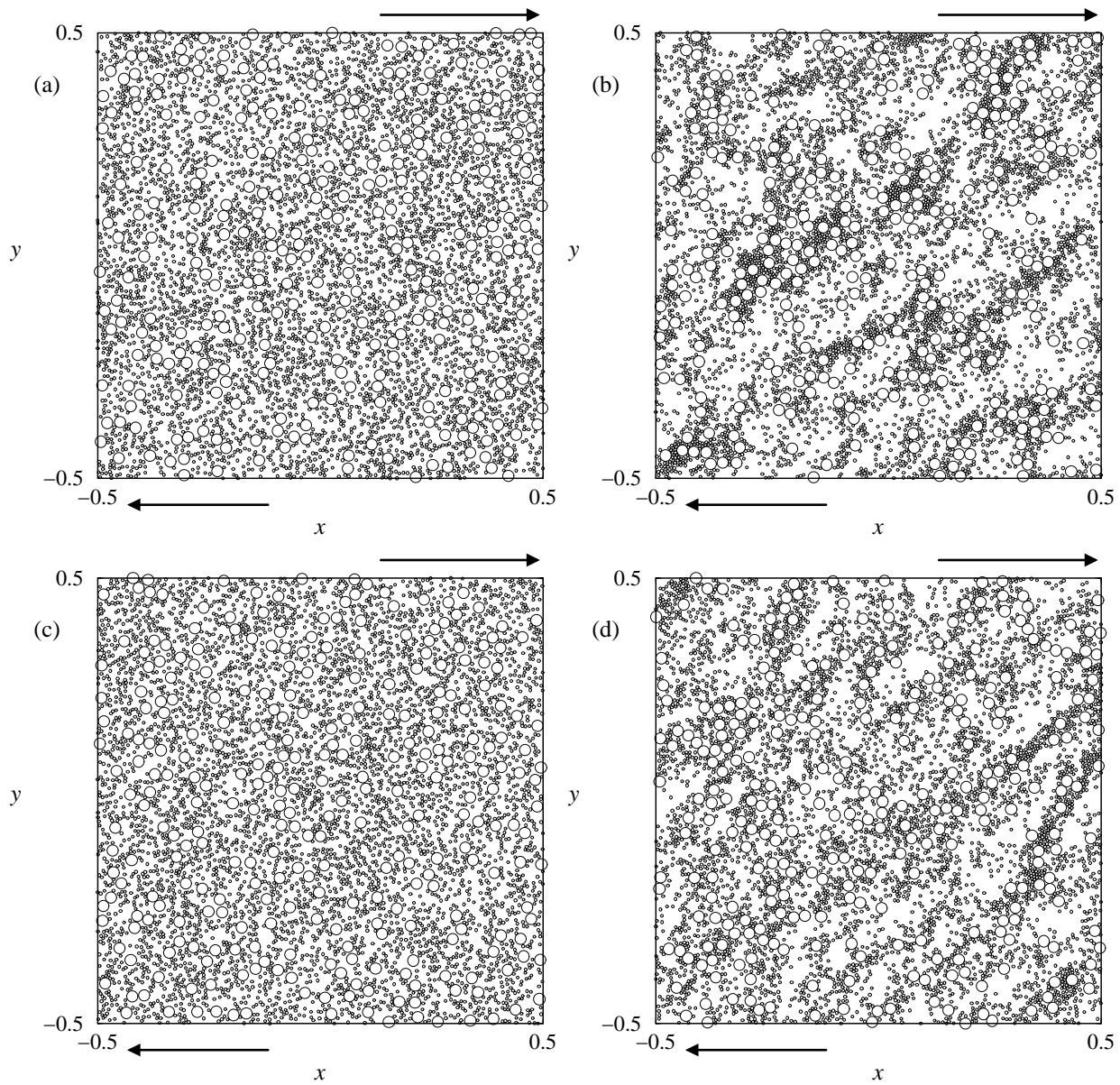
Figure 8, Alam, Physics of Fluids

1

(a)

(b)
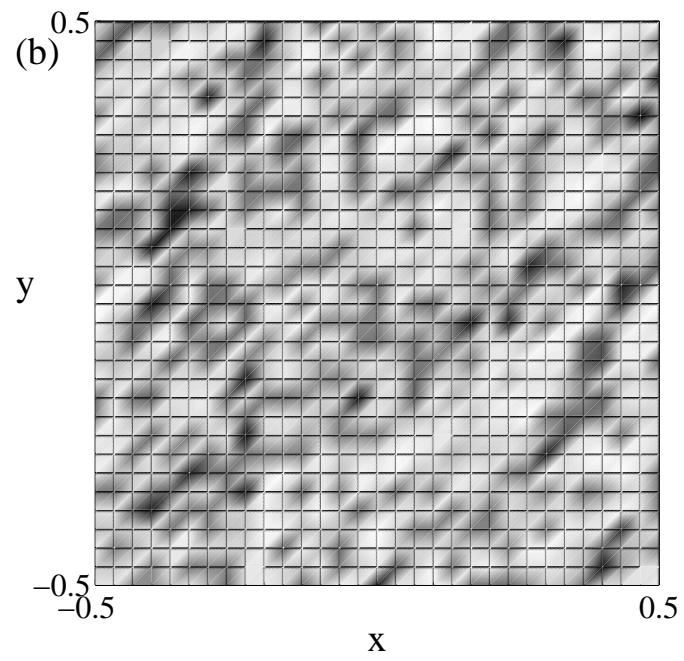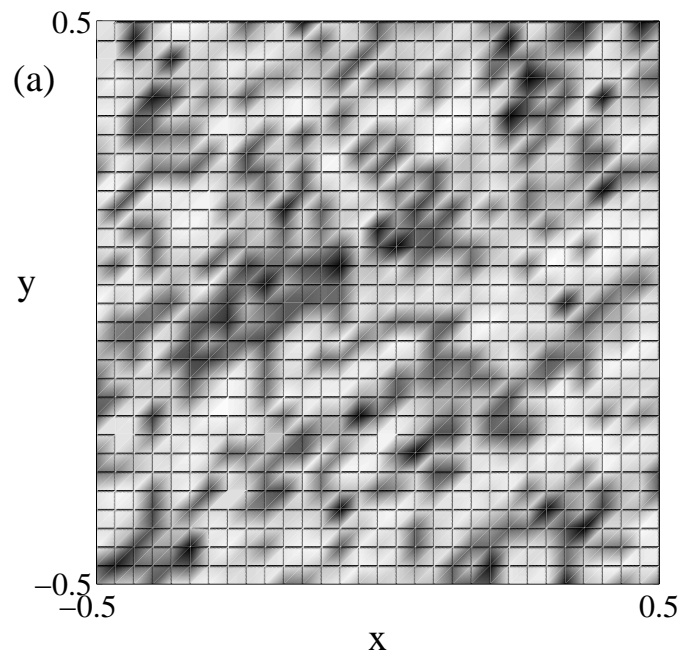
Figure 9, Alam, Physics of Fluids
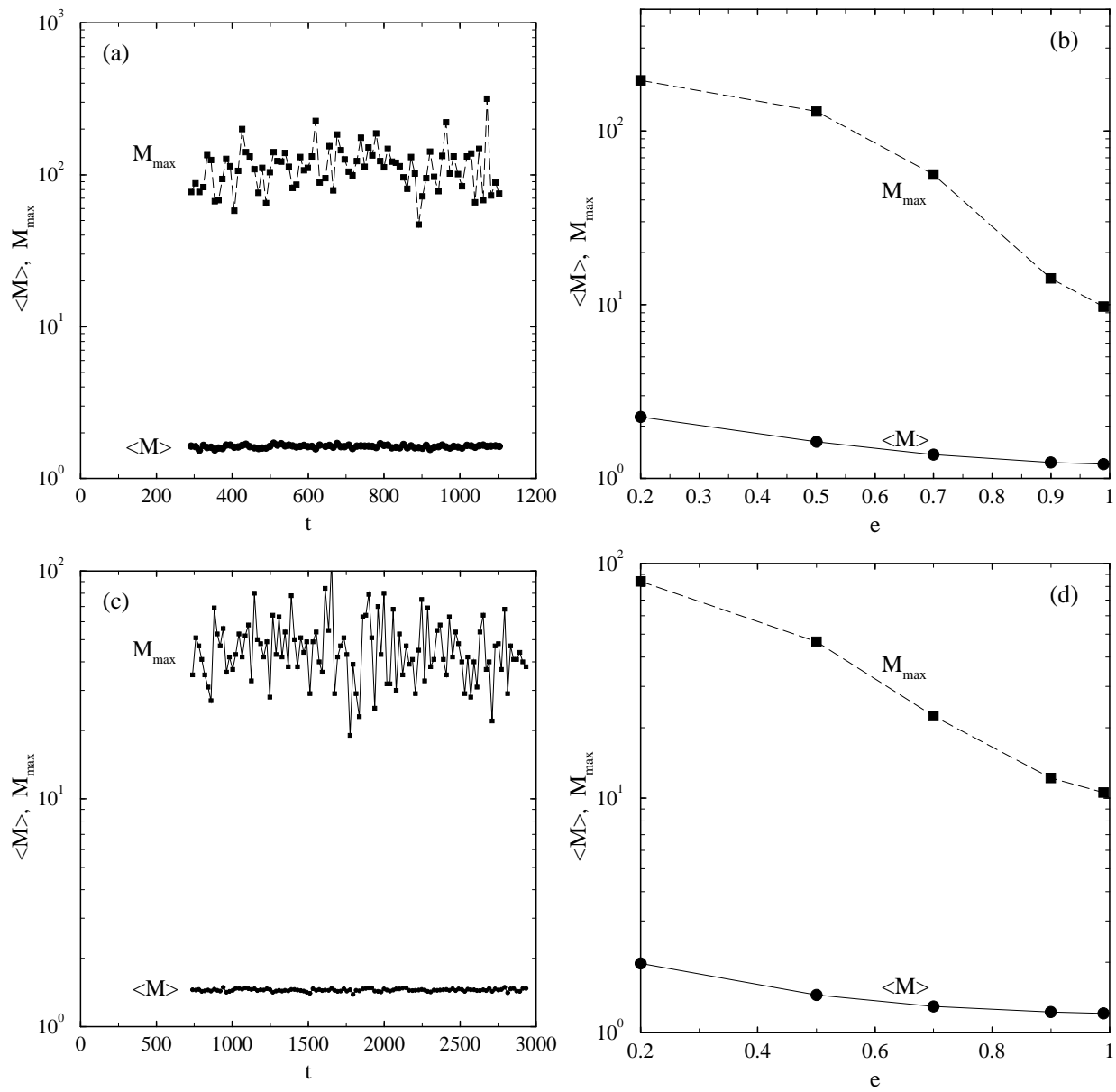
Figure 10, Alam, Physics of Fluids

Rigid Rotation   Pure Straining Motion
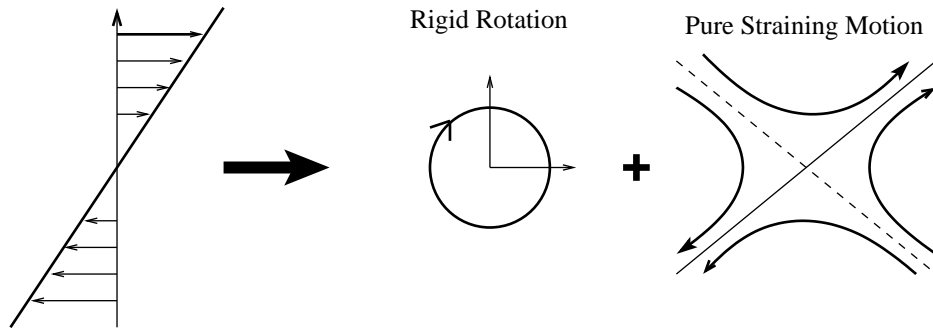
Figure 11, Alam, Physics of Fluids
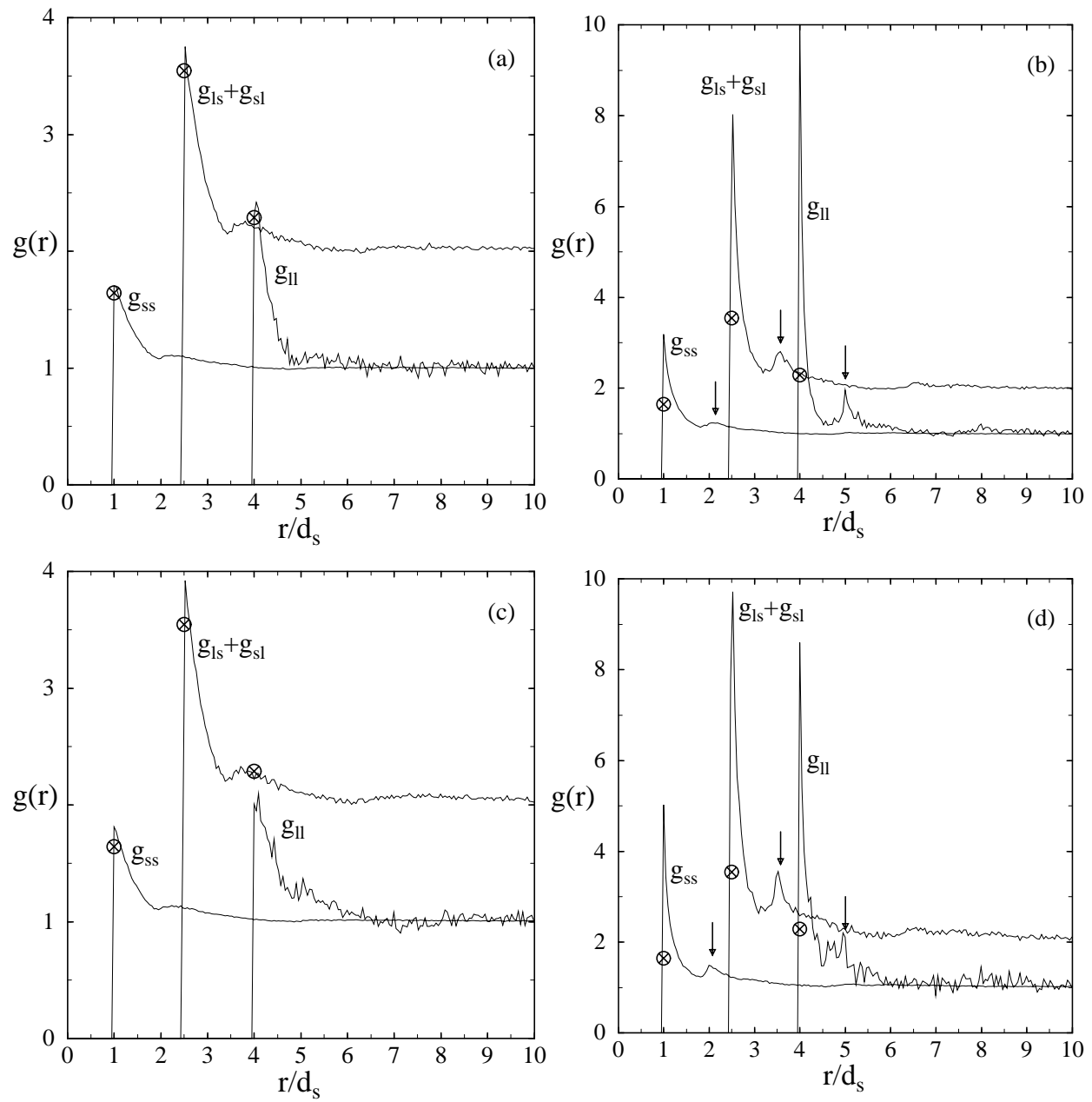
Figure 12, Alam, Physics of Fluids

1
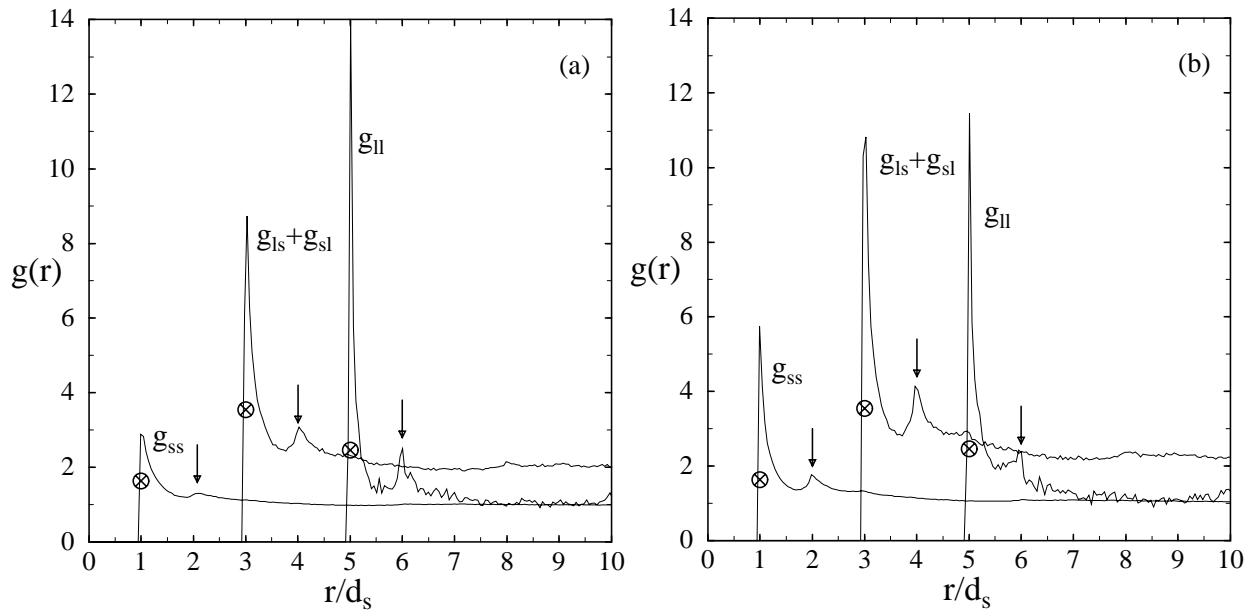
Figure 13, Alam, Physics of Fluids

1
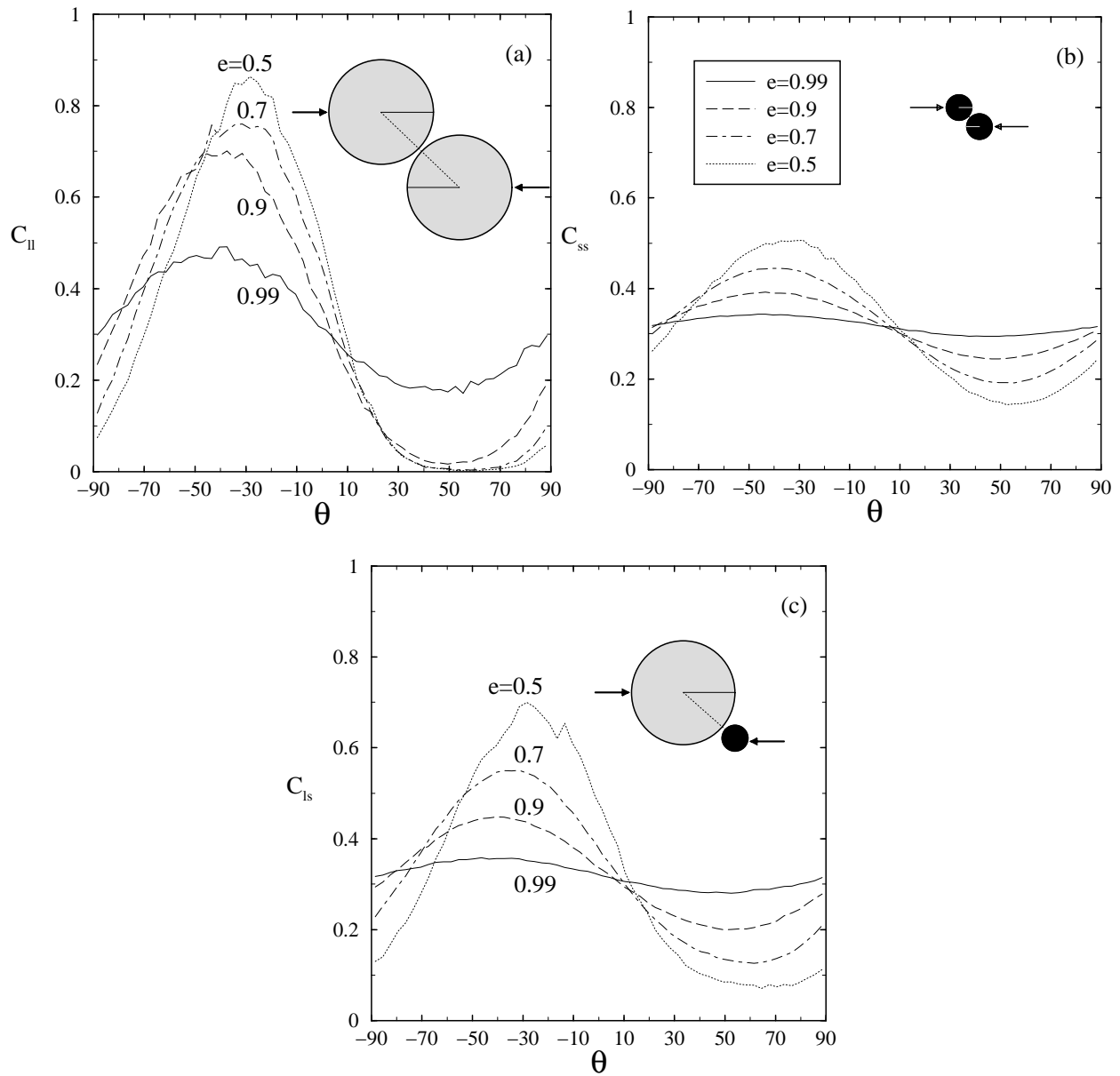
Figure 14, Alam, Physics of Fluids

1
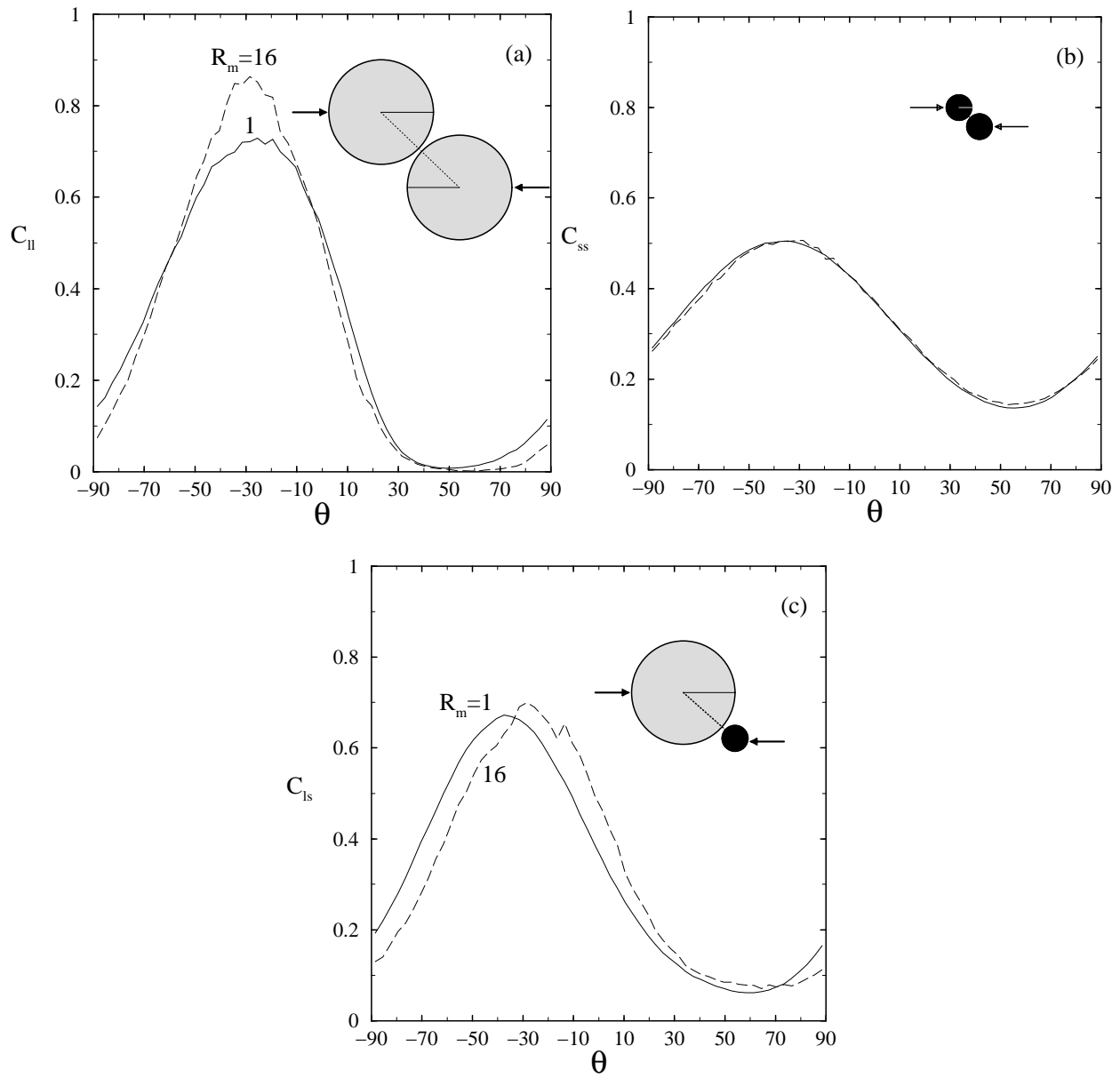
Figure 15, Alam, Physics of Fluids

1